



**HAL**  
open science

## **Polarization from Aligned Dust Grains in the $\beta$ Pic Debris Disk**

Charles L. H. Hull, Haifeng Yang, Paulo C. Cortés, William R. F. Dent, Quentin Kral, Zhi-Yun Li, Valentin J. M. Le Gouellec, A. Meredith Hughes, Julien Milli, Richard Teague, et al.

### ► To cite this version:

Charles L. H. Hull, Haifeng Yang, Paulo C. Cortés, William R. F. Dent, Quentin Kral, et al.. Polarization from Aligned Dust Grains in the  $\beta$  Pic Debris Disk. *The Astrophysical Journal*, 2022, 930, <10.3847/1538-4357/ac6023>. <insu-03705351>

**HAL Id: insu-03705351**

**<https://insu.hal.science/insu-03705351v1>**

Submitted on 27 Jun 2022

HAL is a multi-disciplinary open access archive for the deposit and dissemination of scientific research documents, whether they are published or not. The documents may come from teaching and research institutions in France or abroad, or from public or private research centers.




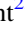






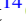
L'archive ouverte pluridisciplinaire HAL, est destinée au dépôt et à la diffusion de documents scientifiques de niveau recherche, publiés ou non, émanant des établissements d'enseignement et de recherche français ou étrangers, des laboratoires publics ou privés.



Distributed under a Creative Commons CC BY 4.0 - Attribution - International License



# Polarization from Aligned Dust Grains in the $\beta$ Pic Debris Disk

Charles L. H. Hull<sup>1,2,15</sup> , Haifeng Yang (杨海峰)<sup>3,4</sup> , Paulo C. Cortés<sup>2,5</sup> , William R. F. Dent<sup>2,6</sup> , Quentin Kral<sup>7</sup> , Zhi-Yun Li<sup>8</sup> , Valentin J. M. Le Gouellec<sup>6,9,10</sup> , A. Meredith Hughes<sup>11</sup> , Julien Milli<sup>12</sup> , Richard Teague<sup>13</sup> , and Mark C. Wyatt<sup>14</sup> 

<sup>1</sup> National Astronomical Observatory of Japan, Los Abedules 3085, Of. 701, Vitacura 763 0414, Santiago, Chile; [chat.hull@nao.ac.jp](mailto:chat.hull@nao.ac.jp)

<sup>2</sup> Joint ALMA Observatory, Alonso de Córdova 3107, Vitacura, Santiago, Chile

<sup>3</sup> Kavli Institute for Astronomy and Astrophysics, Peking University, Yi He Yuan Lu 5, Haidian Qu, Beijing 100871, People's Republic of China  
[hfyang@pku.edu.cn](mailto:hfyang@pku.edu.cn)

<sup>4</sup> Institute for Advanced Study, Tsinghua University, Beijing, 100084, People's Republic of China

<sup>5</sup> National Radio Astronomy Observatory, 520 Edgemont Road, Charlottesville, VA 22903, USA

<sup>6</sup> European Southern Observatory, Alonso de Córdova 3107, Vitacura, Santiago, Chile

<sup>7</sup> LESIA, Observatoire de Paris, Université PSL, CNRS, Sorbonne Université, Université Paris Diderot, Sorbonne Paris Cité, 5 place Jules Janssen, F-92195, Meudon, France

<sup>8</sup> Department of Astronomy, University of Virginia, Charlottesville, VA 22903, USA

<sup>9</sup> SOFIA Science Center, Universities Space Research Association, NASA Ames Research Center, Moffett Field, California 94035, USA

<sup>10</sup> Université Paris-Saclay, CNRS, CEA, Astrophysique, Instrumentation et Modélisation de Paris-Saclay, F-91191, Gif-sur-Yvette, France

<sup>11</sup> Department of Astronomy, Van Vleck Observatory, Wesleyan University, 96 Foss Hill Drive, Middletown, CT 06459, USA

<sup>12</sup> Université Grenoble Alpes, IPAG, F-38000 Grenoble, France

<sup>13</sup> Center for Astrophysics | Harvard & Smithsonian, 60 Garden Street, Cambridge, MA 02138, USA

<sup>14</sup> Institute of Astronomy, University of Cambridge, Madingley Road, Cambridge CB3 0HA, UK

Received 2022 January 21; revised 2022 March 10; accepted 2022 March 21; published 2022 May 3

## Abstract

We present 870  $\mu\text{m}$  Atacama Large Millimeter/submillimeter Array polarization observations of thermal dust emission from the iconic, edge-on debris disk  $\beta$  Pic. While the spatially resolved map does not exhibit detectable polarized dust emission, we detect polarization at the  $\sim 3\sigma$  level when averaging the emission across the entire disk. The corresponding polarization fraction is  $P_{\text{frac}} = 0.51\% \pm 0.19\%$ . The polarization position angle  $\chi$  is aligned with the minor axis of the disk, as expected from models of dust grains aligned via radiative alignment torques (RAT) with respect to a toroidal magnetic field ( $B$ -RAT) or with respect to the anisotropy in the radiation field ( $k$ -RAT). When averaging the polarized emission across the outer versus inner thirds of the disk, we find that the polarization arises primarily from the SW third. We perform synthetic observations assuming grain alignment via both  $k$ -RAT and  $B$ -RAT. Both models produce polarization fractions close to our observed value when the emission is averaged across the entire disk. When we average the models in the inner versus outer thirds of the disk, we find that  $k$ -RAT is the likely mechanism producing the polarized emission in  $\beta$  Pic. A comparison of timescales relevant to grain alignment also yields the same conclusion. For dust grains with realistic aspect ratios (i.e.,  $s > 1.1$ ), our models imply low grain-alignment efficiencies.

*Unified Astronomy Thesaurus concepts:* A stars (5); Debris disks (363); Dust continuum emission (412); Interferometry (808); Interplanetary dust (821); Interplanetary magnetic fields (824); Polarimetry (1278); Submillimeter astronomy (1647); Radiative transfer simulations (1967); Theoretical models (2107)

*Supporting material:* data behind figure

## 1. Introduction

One of the long-standing goals of disk enthusiasts has been to make a well resolved map of the magnetic field in a protoplanetary disk. The detection of polarization in a disk from dust grains aligned with the magnetic field (Lazarian 2007) as a result of the Radiative Alignment Torque mechanism (RAT; Lazarian & Hoang 2007a) would provide evidence that young protostellar disks are magnetized; this is a prerequisite for the operation of the magneto-rotational instability (MRI; Balbus & Hawley 1991) and magnetized disk winds (Blandford & Payne 1982), both of which are thought to play a crucial role in disk evolution. While there

have been a few mid-infrared detections of polarization from magnetically aligned dust grains in disks around Herbig Ae/Be stars (Li et al. 2016, 2018), most of the Atacama Large Millimeter/submillimeter Array (ALMA) observations of thermal dust polarization in disks, primarily at wavelengths of 1.3 mm or 850  $\mu\text{m}$ , can be interpreted as arising from scattering by dust grains (Stephens et al. 2014; Fernández-López et al. 2016; Kataoka et al. 2016; Stephens et al. 2017; Bacciotti et al. 2018; Lee et al. 2018; Girart et al. 2018; Hull et al. 2018; Ohashi et al. 2018; Dent et al. 2019; Harrison et al. 2019; Vlemmings et al. 2019; Ohashi et al. 2020; Teague et al. 2021), consistent with theoretical predictions (e.g., Cho & Lazarian 2007; Kataoka et al. 2015; Yang et al. 2016a). Observations of spectral-line polarization from the Goldreich-Kylafis effect (Goldreich & Kylafis 1981, 1982) offer an alternative way to probe the magnetic field in disks; however, searches for polarized spectral-line emission in bright, nearby Class II disks have thus far yielded either nondetections (Stephens et al. 2020) or very low-level detections whose

<sup>15</sup> NAOJ Fellow.

corresponding magnetic field morphologies were not easy to constrain (Teague et al. 2021).

The young, Class I and II protoplanetary disks toward which polarization from scattering is predominant are thought to be optically thick in the (sub)millimeter regime (Carrasco-González et al. 2016, 2019; Zhu et al. 2019), which is conducive to producing a detectable level of scattering-induced polarization. Consequently, the targets with the best potential for allowing us to minimize the contribution from scattering and detect polarization from magnetically aligned dust grains—thus allowing us to constrain the magnetic field in a solar system precursor—are debris disks, which are optically thin in continuum emission at millimeter wavelengths.

Debris disks are tenuous, dust-dominated circumstellar disks analogous to the solar system’s Kuiper Belt and zodiacal light (Hughes et al. 2018). The existence of debris disks was first inferred from observations by the IRAS satellite that showed infrared excesses around a number of stars including, among others,  $\beta$  Pictoris ( $\beta$  Pic),  $\alpha$  Lyrae (Vega),  $\alpha$  Piscis Austrini (Fomalhaut), and  $\epsilon$  Eridani (Aumann et al. 1984; Aumann 1985).  $\beta$  Pic<sup>16</sup> was the first debris disk to be imaged at optical wavelengths (Smith & Terrile 1984).

$\beta$  Pic is a main-sequence A-type (A6V) star with an effective temperature of 8052 K (Gray et al. 2006); a mass and radius of  $1.797 \pm 0.035 M_{\odot}$  and  $1.497 \pm 0.25 R_{\odot}$ , respectively (Zwintz et al. 2019); and a bolometric luminosity of  $8.7 L_{\odot}$  (Crifo et al. 1997).  $\beta$  Pic is located in the southern constellation of Pictor at a distance of  $19.44 \pm 0.05$  pc (van Leeuwen 2007; using Hipparcos data). The age of the  $\beta$  Pic moving group (and thus of  $\beta$  Pic itself) is calculated to be  $18.5^{+2.0}_{-2.4}$  Myr (Miret-Roig et al. 2020).

$\beta$  Pic hosts a large, bright, edge-on debris disk with a major axis extent of  $\sim 3000$  au when observed at optical wavelengths (Larwood & Kalas 2001); the millimeter-wavelength observations that we present here (and others in the literature, e.g., Wilner et al. 2011; Dent et al. 2014), which trace larger dust grains, reveal a disk diameter of  $\sim 300$  au. The position angle of the major axis of the disk (measured east of north) is approximately  $31^{\circ}$ . The millimeter-wave dust emission has been resolved vertically (i.e., along the minor axis) by previous ALMA observations (Matrà et al. 2019; see also Footnote 5). Optical images of  $\beta$  Pic show a warped inner disk (e.g., Mouillet et al. 1997; Heap et al. 2000; Apai et al. 2015), which has been attributed to possible perturbations by planetary companions. And indeed, two giant planets have been directly observed orbiting the central star:  $\beta$  Pic b (Lagrange et al. 2010) and  $\beta$  Pic c (Lagrange et al. 2019, 2020; Nowak et al. 2020).

The  $\beta$  Pic debris disk is known to be gas rich. Emission has been detected from many atomic and molecular species including, e.g., CO and CI at (sub)millimeter wavelengths (Dent et al. 2014; Kral et al. 2016; Matrà et al. 2017; Cataldi et al. 2018); C II and O I in the far infrared (Cataldi et al. 2014; Brandeker et al. 2016; Kral et al. 2016); Na I, Fe I, and Ca II in the optical (Olofsson et al. 2001; Nilsson et al. 2012); and CO, O I, C I, C II, and C III in the far ultraviolet (Roberge et al. 2000, 2006). The total gas quantity in  $\beta$  Pic is lower than in protoplanetary disks; however, recent studies suggest that the gas may evolve viscously due to the MRI, which may be more active in debris disks than in protoplanetary disks and may operate in a different regime, i.e., one dominated by ambipolar

diffusion (Kral & Latter 2016). A better knowledge of the magnetic field in  $\beta$  Pic would help us better understand whether the MRI can indeed function and explain the system’s gas distribution (Kral et al. 2016).

While there have been many optical and near-infrared observations of debris disks that probe polarization from Rayleigh or Mie scattering by small ( $\sim 0.1$ – $5 \mu\text{m}$ ) dust grains, there is little evidence of polarization from aligned dust grains in debris disks. To our knowledge, the only detection of such polarization is toward the debris disk BD +31°643, whose polarized emission at optical wavelengths may be due to a combination of polarization from scattering and from dichroic extinction by dust grains aligned with a toroidal magnetic field in the disk (Andersson & Wannier 1997). In this work we use  $870 \mu\text{m}$  ALMA polarization observations of thermal dust emission from  $\beta$  Pic to search for polarization from aligned dust grains.

Below, we describe our observations (Section 2) and our main results, which feature, most notably, a detection of polarized dust continuum emission when averaging over the entire disk of  $\beta$  Pic (Section 3). We continue with an exploration of dust-grain alignment models in an attempt to explain the low level of polarized emission that we see toward  $\beta$  Pic. We begin with an introduction to the debris disk model that we employ (Section 4), first in a simple radiative transfer model that we use to constrain the expected intrinsic polarization fraction of emission from aligned dust grains given our observations (Section 5), and next in a more detailed synthetic observation, which fits our ALMA observations well (Section 6). We use the results from these models to constrain current models of dust-grain populations in debris disks (Section 7). Next we explore our results in the context of grain-alignment theory (Section 8). Finally, we discuss the implications of these findings and offer concluding thoughts (Section 9).

## 2. Observations and Imaging

We present ALMA linear-polarization observations of  $\beta$  Pic taken at Band 7 ( $870 \mu\text{m}$ ) with the 12 m array. The data were taken in two sessions: first on 2019 December 18 under good weather conditions (precipitable water vapor [PWV] of 1.03–1.11 mm and a phase rms of 19–22  $\mu\text{m}$ ), with 42 antennas; and again on December 19 under improved conditions (PWV of 0.72–0.93 mm and a phase rms of 18–59  $\mu\text{m}$ ), with 43 antennas. During the observations the antennas were in the C-1 configuration, which has baseline lengths ranging from 14 to 312 m. These baselines allow the recovery of emission up to angular scales as large as  $\sim 7''.9$  and yield a synthesized beam (resolution element) in the combined data set with dimensions of  $1''.08 \times 0''.88$  and a position angle of  $-74.3^{\circ}$  when imaged with a Briggs weighting parameter of  $\text{robust} = 2.0$  (i.e., natural weighting). This average angular resolution of  $0''.97$  corresponds to a spatial resolution of approximately 19 au at the distance to  $\beta$  Pic of 19.44 pc.

The following calibrators were included in the observations: J0522-3627 (polarization and pointing), J0538-4405 (bandpass and flux), and J0526-4830 (complex gain). The two sessions had sufficient parallactic angle coverage of the polarization calibrator ( $118^{\circ}$  and  $116^{\circ}$  in the first and second sessions, respectively), which allowed us to perform polarization calibration (see below). The total on-source time was

<sup>16</sup> Throughout this paper we will use the name  $\beta$  Pic to refer both to the central star and to the debris disk surrounding it.

approximately 189 min, yielding a thermal noise level (i.e., sensitivity) of  $12.8 \mu\text{Jy beam}^{-1}$ .

Our observations used the standard correlator configuration for ALMA Band 7 wide-band continuum (TDM) polarization observations, which includes 8.0 GHz of bandwidth ranging in frequency from  $\sim 337.5\text{--}341.5$  GHz and  $\sim 347.5\text{--}351.5$  GHz, with an average frequency of 344.5 GHz (870  $\mu\text{m}$ ). Each 2 GHz spectral window (with 1.875 GHz of usable bandwidth) is divided into 64 channels with widths of 31.25 MHz.

We obtained the raw data before the data were processed by the ALMA East Asian ALMA Regional Center (EA ARC), and thus we performed our own calibration of the data using version 5.6.1-8 of the Common Astronomy Software Applications (CASA; McMullin et al. 2007) by following recent versions of the standard ALMA pipeline and polarization calibration scripts. For a detailed description of the ALMA polarization calibration procedure, see Nagai et al. (2016). The data were later reduced by the EA ARC staff, whose results matched our own.

In their combined study of Gaia and Hipparcos data, Snellen & Brown (2018) derived the proper motion  $\mu$  of  $\beta$  Pic:  $\mu_{\text{R.A.}} = 4.94 \pm 0.02 \text{ mas yr}^{-1}$  and  $\mu_{\text{decl.}} = 83.93 \pm 0.02 \text{ mas yr}^{-1}$ , very similar to the values derived from the Hipparcos-only data (van Leeuwen 2007). The ICRS coordinates of  $\beta$  Pic measured from the second Gaia data release (DR2; Gaia Collaboration et al. 2018) in epoch 2015.5 (i.e., its position on approximately 2015 June 30) were  $(\alpha, \delta) = (05:47:17.0960784 \pm 0.315 \text{ mas}, -51:03:58.132908 \pm 0.342 \text{ mas})$  (Snellen & Brown 2018). Using the proper motions from Snellen & Brown, we can extrapolate from the Gaia DR2 position to the position of  $\beta$  Pic in our Band 7 data observed in mid-December of 2019. The resulting position matches the position of the central peak in our 2019 Band 7 image to within the  $\sim 100$  mas positional uncertainty in our fits, which is due to the low resolution of our data and the extended nature of the emission toward  $\beta$  Pic. We thus choose to use the position of  $\beta$  Pic extrapolated from the proper motions as the position of the source (i.e., the position of the central star) at the time of our Band 7 observations. That position in J2000 coordinates is  $(\alpha, \delta) = (05^{\text{h}}47^{\text{m}}17^{\text{s}}.098, -51^{\circ}03'57''.758)$ . We use the CASA task FIXVIS to redefine the phase center of our observations, fixing it to the aforementioned position. We then use the CASA task FIXPLANETS to set the coordinates of the phase center to be equal to that position; this latter step converts the coordinates from ICRS (the current default ALMA coordinate system) to J2000.

Because the  $\sim 15''$  angular extent of  $\beta$  Pic nearly fills the  $\sim 18''$  field of view (also known as the “primary beam”; the reported extent of the field of view represents the full-width at half-maximum, or FWHM) of the ALMA 12 m antennas at Band 7, we observed  $\beta$  Pic in three separate pointings: one centered on the location of the central star  $\beta$  Pic and two located  $\sim 3.5''$  along the major axis in the NE and SW directions. When making our final images, we combine the data from all three pointings in a mosaic. The  $1\sigma$  systematic uncertainty in polarization fraction for a single-pointing, on-axis linear polarization observations with ALMA is 0.03% of Stokes  $I$  (corresponding to a minimum detectable polarization fraction of 0.1%). The  $1\sigma$  systematic errors increase to  $\sim 0.5\%$  near the FWHM of the primary beam in Band 7 observations; however, these errors are reduced by mosaicking (Hull et al. 2020; Cortes et al. 2021). Furthermore, the off-axis errors within the inner  $\frac{1}{3}$  of the FWHM at Band 7 are at most 0.1% (Hull et al. 2020), and our small mosaic has been

**Table 1**  
Full-disk-averaged Data

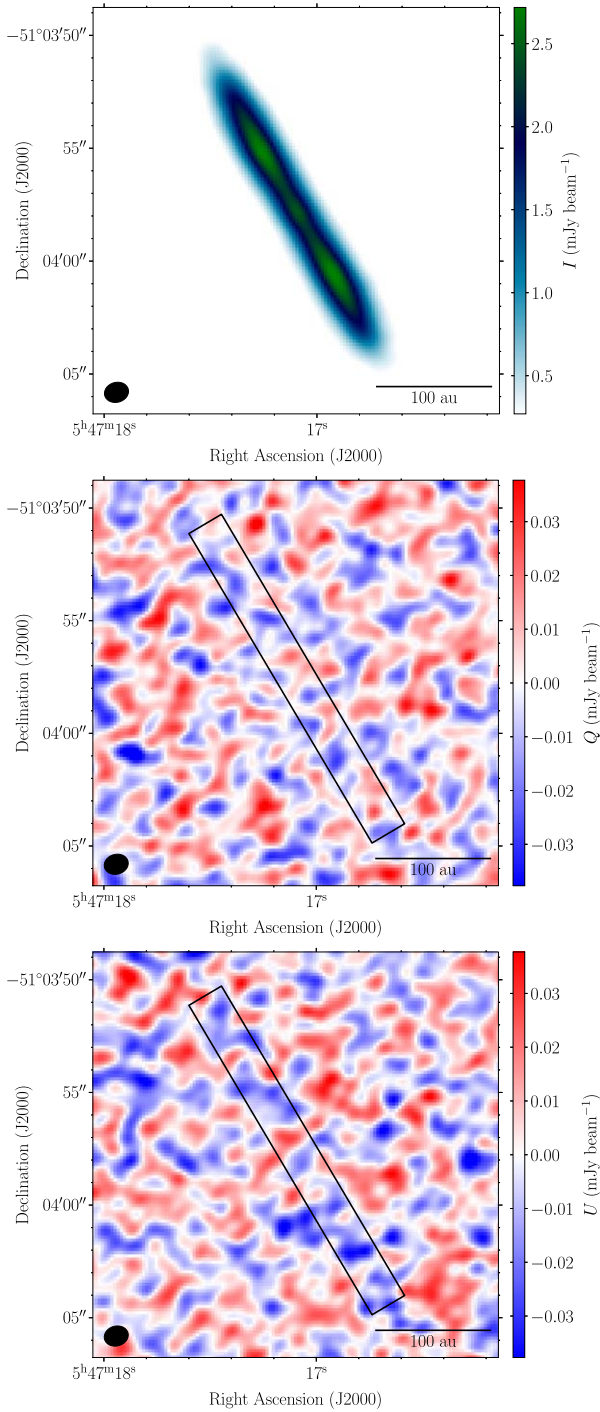
Quantity	Value
$I$	$1368 \mu\text{Jy beam}^{-1}$
$Q$	$-4.0 \mu\text{Jy beam}^{-1}$ (S/N = 1.5)
$U$	$-6.9 \mu\text{Jy beam}^{-1}$ (S/N = 2.7)
$\chi$	$-59.9 \pm 10.6^\circ$
$Q'$	$8.0 \mu\text{Jy beam}^{-1}$ (S/N = 3.1)
$U'$	$-1.5 \mu\text{Jy beam}^{-1}$ (S/N = 0.1)
$\chi'$	$-0.5 \pm 10.6^\circ$
$P$	$6.9 \mu\text{Jy beam}^{-1}$ (S/N = 2.7)
$P_{\text{frac}}$	$0.51\% \pm 0.19\%$

**Note.** All flux density values have been averaged across the brightest part of the  $\beta$  Pic debris disk, as described in Section 3.1.  $Q'$ ,  $U'$ , and  $\chi'$  reflect the values after performing the transformation described in Equations (9) and (10). The value of the polarized intensity  $P$  is debiased as described in Section 2. All S/N values are calculated using the rms noise value of  $2.6 \mu\text{Jy beam}^{-1}$  from the full-box-averaged  $Q$ ,  $U$ , and debiased  $P$  maps (see Section 3.1). For reference, the position angle of the minor axis of the disk is  $-59^\circ$  in the original reference frame and  $0^\circ$  in the rotated reference frame.

setup so that all of the emission from the  $\beta$  Pic disk falls within the inner  $\frac{1}{3}$  of one of the three pointings; the systematic errors in polarization fraction are thus approximately  $2 \times$  smaller than the statistical errors in our measurements (see Sections 3 and Table 1).

We use the task TCLEAN from CASA version 6.4.0.16 to produce images of  $\beta$  Pic, including of Stokes  $I$ , which corresponds to the total intensity dust emission, and of Stokes  $Q$  and  $U$ , which correspond to linearly polarized emission. We first make dirty images (i.e., with 0 clean iterations, corresponding to the source emission convolved with the ALMA point-spread function [PSF], or “dirty beam”) of all three Stokes parameters. It is at this step that we find that  $Q$  and  $U$  do not show any obvious emission; therefore, we do not clean  $Q$  and  $U$  further. However, as Stokes  $I$  exhibits ample signal, we clean the map using the TCLEAN auto-masking function (keyword: auto-multithresh) and performing 3225 iterations to clean down to a threshold of  $16 \mu\text{Jy beam}^{-1}$ . Both the residual and final images of Stokes  $I$  exhibit large-scale positive and negative ripples in the map at the  $\pm 200 \mu\text{Jy beam}^{-1}$  level (i.e., approximately  $\pm 10\%$  of the peak Stokes  $I$  level), suggesting that our observations are unable to recover large-scale emission in the field of view (single-dish observations have shown continuum emission extending along the major axis to scales greater than the  $\sim 20''$  scales probed by our ALMA observations; Liseau et al. 2003). We are not able to reduce these features by self-calibrating the data, as the signal-to-noise ratio (S/N) of the Stokes  $I$  emission is too low. We thus proceed with the final images of the non-self-calibrated data despite the systematic ripples. We should note, however, that these features do not affect our analysis, most of which hinges on the  $Q$  and  $U$  maps, which exhibit no such features and which achieve the expected thermal noise level of the observations. The `robust = 2.0` maps that we analyze in the following sections are shown in Figure 1.

The rms noise level in the dynamic-range-limited Stokes  $I$  dust map is  $28.1 \mu\text{Jy beam}^{-1}$ , calculated using the `sigma_clipped_stats` function from the `stats` module of the `astropy` Python package (Astropy Collaboration et al. 2018). The rms noise levels in the dirty  $Q$  and  $U$  images are



**Figure 1.** 870  $\mu\text{m}$  total intensity (Stokes  $I$ , top) and polarization (Stokes  $Q$ , center; and  $U$ , bottom) maps of the  $\beta$  Pic debris disk. The Stokes  $I$  map is dynamic-range limited, and is plotted beginning at  $10 \times$  the rms noise level of  $28.1 \mu\text{Jy beam}^{-1}$ . The peak of the Stokes  $I$  emission is  $2.59 \text{ mJy beam}^{-1}$ . The Stokes  $I$  image has been corrected for the primary beam response; the integrated flux is  $47 \text{ mJy}$ . The  $Q$  and  $U$  maps are noise like and are plotted between  $\pm 3 \times$  the average rms noise level in the  $Q$  and  $U$  maps of  $12.8 \mu\text{Jy beam}^{-1}$ . The  $Q$  and  $U$  maps have not been primary-beam corrected. The synthesized beam (resolution element) is shown as a black ellipse in the bottom-left corner of each panel and has dimensions of  $1''.08 \times 0''.88$  and a position angle of  $-74.3^\circ$ . The rectangles in the  $Q$  and  $U$  images indicate the region where we average the  $Q$  and  $U$  emission (see Section 3).

(The data used to create this figure are available.)

$13.0 \mu\text{Jy beam}^{-1}$  and  $12.6 \mu\text{Jy beam}^{-1}$ , respectively, consistent with the thermal noise level expected given the on-source observation time.

The Stokes  $I$  flux density of  $\beta$  Pic derived using the primary-beam-corrected maps from our 2019 data is approximately  $47 \text{ mJy}$ . This value is significantly lower than the  $60 \text{ mJy}$  value quoted by Dent et al. (2014); however, our value is consistent with the automated result from the Japanese Virtual Observatory (JVO)<sup>17</sup> using the same data reported in Dent et al., and with the flux values in the images provided by the EA ARC when they delivered our data. We thus assume that our derived flux value is correct.

The quantities (and upper limits) that can be derived from Stokes  $I$ ,  $Q$ , and  $U$  maps include the polarized intensity  $P$ , the linear polarization fraction  $P_{\text{frac}}$ , and the polarization position angle  $\chi$  (measured E of N):

$$P = \sqrt{Q^2 + U^2} \quad (1)$$

$$P_{\text{frac}} = \frac{P}{I} \quad (2)$$

$$\chi = \frac{1}{2} \arctan\left(\frac{U}{Q}\right). \quad (3)$$

As  $P$  is always a positive quantity (unlike the  $Q$  and  $U$  maps from which  $P$  is derived, which can be either positive or negative), it has a positive bias. This bias is particularly significant in low-S/N measurements like those we report here. We debias the polarized intensity values as described in Wardle & Kronberg (1974), Hull & Plambeck (2015), Teague et al. (2021). Note that to debias a polarized intensity  $P$  map one must use the rms noise value in the corresponding nondebaised  $P$  map. After debiasing the  $P$  map, the rms noise value of the  $P$  map becomes approximately equal to the noise values in the  $Q$  and  $U$  maps.

The statistical uncertainties  $\sigma_I$ ,  $\sigma_Q$ ,  $\sigma_U$ , and  $\sigma_P$  in the  $I$ ,  $Q$ ,  $U$ , and debaised  $P$  maps are all equal to the rms noise values in the respective maps. The uncertainty  $\sigma_\chi$  in the polarization position angle  $\chi$  is:

$$\sigma_\chi = \frac{1}{2} \frac{\sqrt{(Q\sigma_U)^2 + (U\sigma_Q)^2}}{P^2} \quad (4)$$

$$\approx \frac{1}{2} \frac{\sigma_P}{P}. \quad (5)$$

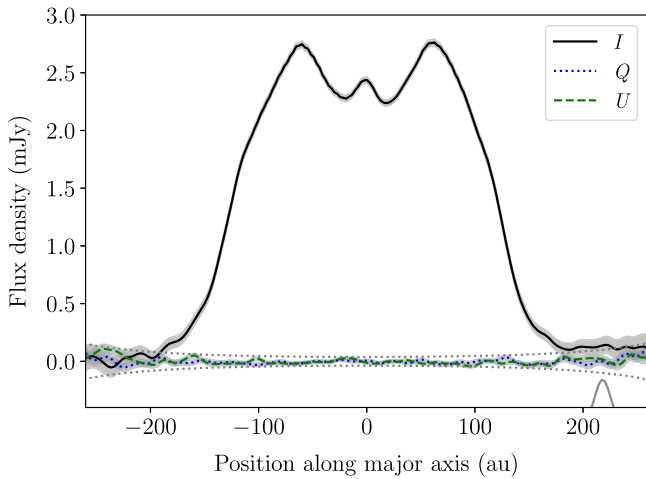
We make the simplification on the second line by assuming that  $\sigma_Q \approx \sigma_U \approx \sigma_P$ . Note that this expression assumes a Gaussian distribution in position angles, which is not the case for low-S/N measurements (Naghizadeh-Khouei & Clarke 1993). We nevertheless proceed with these expressions to derive first-order estimates of the uncertainties in  $\chi$ , which are sufficient for our analysis.

The uncertainty  $\sigma_{P_{\text{frac}}}$  in the polarization fraction  $P_{\text{frac}}$  is:

$$\sigma_{P_{\text{frac}}} = P_{\text{frac}} \sqrt{\left(\frac{\sigma_P}{P}\right)^2 + \left(\frac{\sigma_I}{I}\right)^2} \quad (6)$$

$$\approx P_{\text{frac}} \frac{\sigma_P}{P} \quad (7)$$

<sup>17</sup> JVO: <http://jvo.nao.ac.jp/portal>.



**Figure 2.** Cuts along the major axis of  $\beta$  Pic. The plot traces emission from the NE on the left (negative major axis values) to the SW on the right (positive values). The images used have been primary-beam corrected, and thus the  $\pm 3\sigma$  limits (dotted gray lines) are curved, increasing toward the edge of the image. A cut through the  $\sim 1''$  synthesized beam (with the  $x$ -axis of the plot positioned at the beam’s FWHM) is shown in the lower-right corner.

$$= \frac{\sigma_P}{I}, \quad (8)$$

where  $P$  is the debiased map of polarized intensity. The simplification on the second line is appropriate for low-S/N data, where  $(\sigma_P/P)^2$  ( $= 0.25$  for  $P = 2\sigma_P$ ) is much larger than  $(\sigma_I/I)^2$  ( $\approx 10^{-4}$  for a Stokes  $I$  S/N of  $\approx 100$  in the brightest regions of  $\beta$  Pic).

### 3. Results

The  $Q$  and  $U$  images of  $\beta$  Pic (see the bottom two panels of Figure 1) show emission consistent with noise. We confirm this in Figure 2, where we show  $I$ ,  $Q$ , and  $U$  cuts along the major axis of the disk. The cuts trace emission from the NE on the left (negative major axis values) to the SW on the right (positive values). The  $Q$  and  $U$  profiles lie between the  $\pm 3\sigma$  curves (since  $Q$  and  $U$  can be positive or negative), where  $\sigma$  is the average rms noise level in the  $Q$  and  $U$  maps. The  $3\sigma$  curves in Figure 2 are curved as a result of the increase in the noise toward the edge of the maps, which (unlike the maps in Figure 1) have been corrected for the primary-beam response of the small mosaic.

In Figure 3, we use the spatially resolved maps shown in Figure 1 to calculate upper limits on the polarization fraction  $P_{\text{frac}}$  along the major axis of  $\beta$  Pic. In the left panel, we plot the  $3\sigma$  upper limits on  $P_{\text{frac}}$ , calculated by dividing  $3 \times$  the off-source rms noise level in the debiased polarized intensity  $P$  map ( $12.8 \mu\text{Jy beam}^{-1}$ ) by the Stokes  $I$  cut from Figure 2. In the right panel, we plot the  $3\sigma$  upper limits on  $P_{\text{frac}}$  after folding the Stokes  $I$  data (i.e., averaging the data mirrored across the minor axis) and using an rms noise level in  $P$  that is  $\sqrt{2}$  lower than the value used in the left panel. The  $P_{\text{frac}}$  upper limits within approximately  $\pm 80$  au of the center of the  $\beta$  Pic debris disk are  $\sim 1.6\%$  (not folded) and  $\sim 1.1\%$  (folded).

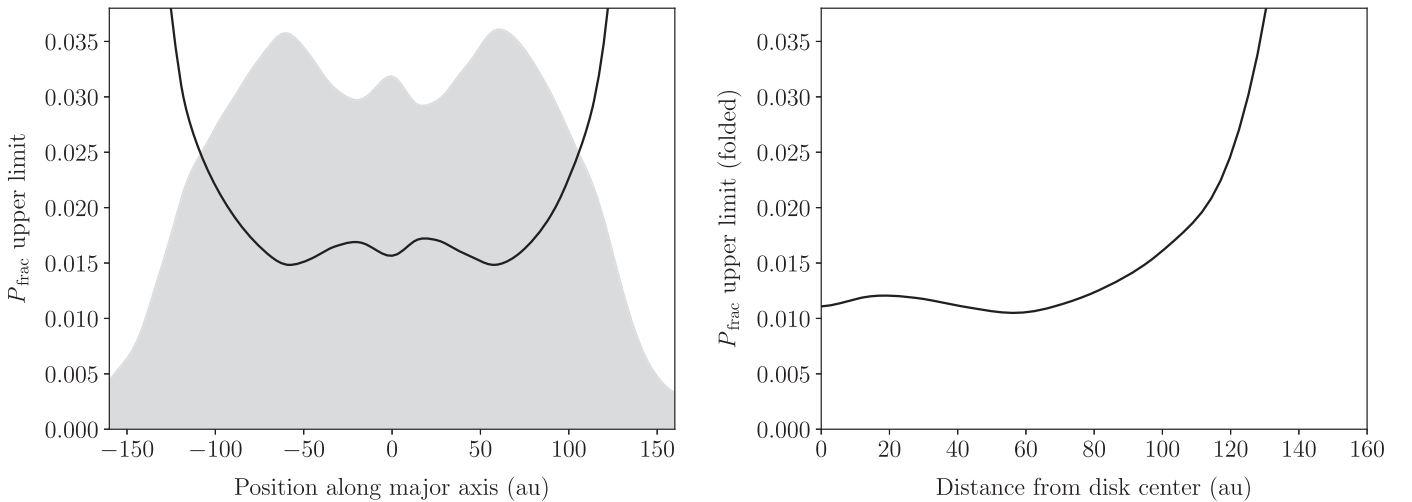
#### 3.1. $\sim 3\sigma$ Detection of Dust Polarization when Averaging Across the Entire Disk of $\beta$ Pic

To search for polarized dust emission below the noise level of the resolved maps, we average the emission across the entire disk of  $\beta$  Pic. The main assumption that we make when performing this averaging is that the position angle of any polarized emission is the same everywhere: i.e., that it does not change as a function of position along either the minor or major axis of the disk. This is reasonable given that, in an edge-on disk, the position angle of polarized dust emission should be uniformly along the minor axis of the disk in all of the following cases: scattering by dust grains (e.g., Lee et al. 2018); dust grains aligned via RATs with a toroidal magnetic field (known hereafter as  $B$ -RAT); and dust grains aligned with the (radial) radiation flux, or, more specifically, anisotropy in the radiation field (known hereafter as  $k$ -RAT; Lazarian & Hoang 2007a; Tazaki et al. 2017). However, as we will see later, there is a key difference in the emission profiles from grains aligned via  $B$ -RAT versus  $k$ -RAT: in the case of  $B$ -RAT, the polarization fraction peaks near the center of the disk, whereas in the case of  $k$ -RAT the polarization fraction peaks near the outer regions of the disk (see Section 5 and Figure 6).

We average the maps using a box with dimensions of  $12 \times 114$  pixels. Each pixel in our maps is  $0''.14$  in size, yielding a box size of  $1''.7 \times 16''.0$ , or  $32.7 \text{ au} \times 310 \text{ au}$ . We perform this averaging on-source as well as in 14 off-source positions, seven on each side of the source. The on-source averaging box covers the brightest part of the disk; we center the box at the position of the central star and set its size to maximize the S/N of the full-disk-averaged value of debiased  $P$ . The off-source boxes are separated in the direction of the minor axis by 7 pixels; as the width of each box is 12 pixels, the sampling of the boxes in the map is slightly higher than Nyquist.

After computing full-disk-averaged values of  $Q$  and  $U$ , we compute the polarized intensity  $P$  (Equation (1)). In order to properly debias the full-disk-averaged  $P$  value (see Section 2) and to calculate S/N values for  $Q$ ,  $U$ , and debiased  $P$ , we need full-disk-averaged rms noise values, which we define to be the rms in the spatially resolved maps ( $18.2 \mu\text{Jy beam}^{-1}$  for nondebiased  $P$ ;  $12.8 \mu\text{Jy beam}^{-1}$  for  $Q$  and  $U$  and debiased  $P$ ) divided by  $\sqrt{30}$ , where 30 is the number of synthesized beam areas contained in the averaging box. The full-disk-averaged noise value for nondebiased  $P$  is  $3.6 \mu\text{Jy beam}^{-1}$ ; for  $Q$  and  $U$  (and debiased  $P$ ), the value is  $2.6 \mu\text{Jy beam}^{-1}$ . We use the former noise value to debias the full-disk-averaged  $P$  value and the latter value to calculate S/N values. We also calculate the polarization fraction  $P_{\text{frac}}$  (Equation (2), using the full-disk-averaged  $I$  and debiased  $P$  values) and position angle  $\chi$  (Equation (3)).

The on-source results are as follows. The S/N of the debiased  $P$  value, defined as  $P$  divided by the full-disk-averaged rms noise, is 2.7, with corresponding  $Q$  and  $U$  S/N values of 1.5 and 2.7, respectively. The polarization fraction  $P_{\text{frac}} = 0.0051 \pm 0.0019$  (i.e.,  $0.51\% \pm 0.19\%$ ) and polarization position angle  $\chi = -59^\circ.9 \pm 10^\circ.6$ . This value of  $\chi$  matches the  $-59^\circ$  position angle of minor axis of  $\beta$  Pic to within the uncertainty of the position angle. We perform the same analysis for all of the 14 off-axis positions. The S/N value of the debiased  $P$  is by far the highest (with an S/N of 2.7) in the on-axis position. Two off-axis positions have debiased  $P$  S/N



**Figure 3.**  $3\sigma$  upper limits on the dust polarization fraction  $P_{\text{frac}}$  in  $\beta$  Pic, where  $\sigma = 12.8 \mu\text{Jy beam}^{-1}$  is the rms noise level in the spatially resolved, debiased  $P$  map. Left: The solid line is the upper limit calculated by dividing  $3\sigma$  by the Stokes  $I$  cut plotted in Figure 2. The plot traces emission from the NE on the left (negative major axis values) to the SW on the right (positive values). The Stokes  $I$  cut is shown in gray for reference, with arbitrary vertical units. Right:  $3\sigma P_{\text{frac}}$  upper limits plotted as a function of distance from the central star in  $\beta$  Pic. We calculate the solid line by folding the Stokes  $I$  data (i.e., averaging the data mirrored across the minor axis), and by using an rms noise level that is  $\sqrt{2}$  lower than what was used in the left panel. Note that the upper limits are reported as fractions, not percentages.

values of 1.9 and 0.8; the remainder of the positions have S/N values of 0.

Finally, in an attempt to achieve a higher-S/N detection from the  $Q$  and  $U$  maps, we transform the  $Q$  and  $U$  data into the  $Q'$  and  $U'$  frame as follows:

$$Q' = Q \cos(2\theta) + U \sin(2\theta), \quad (9)$$

$$U' = U \cos(2\theta) - Q \sin(2\theta), \quad (10)$$

where  $\theta = 90^\circ - 31^\circ$ ; the latter angle ( $31^\circ$ ) is the orientation of the major axis of the disk. In the transformed ( $Q'$ ,  $U'$ ) reference frame,  $+Q'$  is oriented along the minor axis of the disk. This transformation is similar to the one used by Schmid et al. (2006), Teague et al. (2021). However, whereas those authors used this method to transform centro-symmetric (e.g., radial or azimuthal) polarization patterns as a function of polar angle on the sky, our application is simpler: we apply the same transformation to each pixel in our images, since the polarization from  $\beta$  Pic is assumed to have the same orientation everywhere in the disk.

Assuming, as we have thus far, that all polarized emission from  $\beta$  Pic should have a position angle along the minor axis of the disk, we would expect the transformed data to exhibit substantial positive signal in  $Q'$ . This is indeed what we find. While the debiased  $P$  value of the transformed data has an identical S/N of 2.7 (as expected), we find that  $Q'$  is positive and has a statistically significant S/N of 3.1.  $U'$  is consistent with noise, and the corresponding position angle  $\chi'$  is consistent with  $0^\circ$  (i.e., along the minor axis of the disk in the transformed reference frame). See Table 1 for a summary of our observational results and Table 2 for a list of noise values relevant to our analysis.

### 3.2. Polarized Dust Emission in the Middle Versus Outer Regions of $\beta$ Pic

Considering the significant detection of polarized emission when averaging across the entire disk, the final tests we perform are to search for polarized emission in the inner region of the disk (where we would expect to see more polarized emission from grains aligned via  $B$ -RAT) versus the outer regions (where polarized emission from grains aligned via  $k$ -

**Table 2**  
rms Noise Values

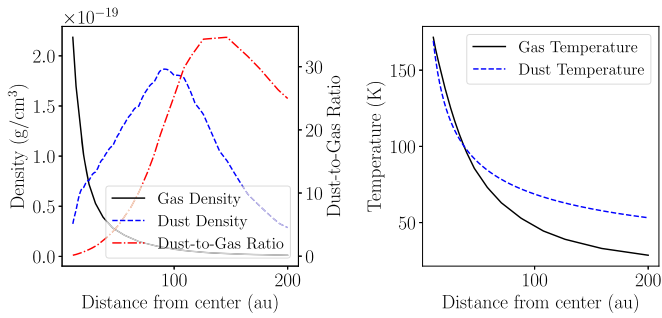
Noise Value ( $\mu\text{Jy beam}^{-1}$ )	Description
28.1	Stokes $I$ noise
12.8	Mean of Stokes $Q$ and $U$ noise
2.6	Mean of full-disk-avg. $Q$ and $U$ noise

**Note.** Relevant noise values. Rows 1–2 are from the spatially resolved maps (Section 3). Row 3 is from the full-disk-averaged maps (Section 3.1). After debiasing  $P$  (whether spatially resolved or full-disk averaged), the noise in the  $P$  map is approximately equal to the noise in the associated  $Q$  and  $U$  maps.

RAT should dominate). We perform our averaging tests using different sections (e.g., quarters, thirds, halves) of a box that is slightly longer than the one used for the full-disk averaging described above. The box has dimensions of  $12 \times 130$  pixels, corresponding to a box size of  $1''.7 \times 18''.2$  or  $32.7 \text{ au} \times 354 \text{ au}$ .

Our first test is to analyze the middle half of the disk versus the (combined) outer two quarters. We do not detect significant polarization in the inner half of the disk centered on the central star of  $\beta$  Pic. However, the combined outer two quarters exhibit polarized emission at the 1.1% level with a marginally significant S/N in the debiased  $P$  map of 2.1 (the S/N in the  $Q'$  map is 2.3). The fact that the polarized emission is only detected in the outer regions of  $\beta$  Pic suggests that dust grains aligned via  $k$ -RAT are producing the polarized emission, as we will discuss later in more detail.

Given that the polarized emission appears to be coming from the outer regions of the disk, our second test is to analyze the NE third, center third, and SW third of the disk separately. We find no detectable polarization in the NE or center thirds; we only detect polarized emission in the SW third in the debiased  $P$  map at the 1.1% level with a marginally significant S/N of 2.4 (the S/N in the  $Q'$  map is 2.8). This asymmetry in the polarized emission is unexpected given the symmetry of the Stokes  $I$  emission in our  $870 \mu\text{m}$  ALMA observations (Figure 1, top panel). However, asymmetries in the Stokes  $I$  dust emission are seen at other wavelengths, from the optical



**Figure 4.** Various radial profiles in our model, based on Zagorovsky et al. (2010), Kral et al. (2016). Left: Gas mass density, dust mass density, and dust-to-gas mass ratio. Right: Gas and dust temperatures.

(Apai et al. 2015) to the mid-infrared (Telesco et al. 2005) to 1.3 mm observations by ALMA; the latter suggest that the dust peak on the SW side of the disk is  $\sim 13\%$  brighter than the NE peak.<sup>18</sup> It is unclear whether the asymmetry seen at other wavelengths is related to the asymmetry in the polarized emission. We leave the topic of asymmetry for future studies, and proceed to interpret our observations using symmetric models. In the sections that follow we endeavor to explain the low level of dust polarization in  $\beta$  Pic by exploring the parameter space of our theoretical models of dust-grain alignment via RATs in a debris disk.

#### 4. Model of the $\beta$ Pic Debris Disk

We use the  $\beta$  Pic debris disk model presented in Kral et al. (2016, hereafter K16; see their Figure 9). In this model, the gaseous component of the disk is composed of carbon and oxygen atoms with equal number densities (unlike typical protoplanetary disks that are dominated by molecular hydrogen,  $\beta$  Pic’s gaseous component is of secondary origin, and the molecular hydrogen density is small: see, e.g., Matrà et al. 2017). We derive the gas mass density  $\rho_g$  and the gas number density  $n_g$  from the O I number density. The dust density  $\rho_d$  is taken from Zagorovsky et al. (2010), who determine it empirically by fitting scattered-light dust observations of  $\beta$  Pic from the Hubble Space Telescope/STIS (Heap et al. 2000).<sup>19</sup> Together, the values of  $\rho_d$  and  $\rho_g$  yield a dust-to-gas mass ratio of up to approximately 30:1, far higher than the typically assumed ratio of 1:100 in protoplanetary disks and in the galactic interstellar medium (Bohlin et al. 1978).  $\rho_d$ ,  $\rho_g$ , and the dust-to-gas ratio are plotted in the left panel of Figure 4.

The gas temperature  $T_g$  and the gas scale height are taken directly from K16, where they are calculated self-consistently via a photodissociation-region model. For simplicity, we assume the dust scale height is the same as that of the gas.<sup>20</sup>

<sup>18</sup> This can be seen in JVO images of 1.3 mm dust continuum observations of  $\beta$  Pic from ALMA project 2018.1.00072.S.

<sup>19</sup> The large, millimeter-sized grains seen by ALMA are located between 50–130 au (Dent et al. 2014). In contrast, the smaller, micron-sized grains seen in scattered light and in the mid-infrared extend from  $<30$  au (originating in a possible inner disk; Li et al. 2012; Apai et al. 2015; Millar-Blanchaer et al. 2015) to beyond 2000 au (because of radiation pressure).

<sup>20</sup> The dust in  $\beta$  Pic most likely resides in more complicated structures than those captured by our simple model. Matrà et al. (2019) modeled the vertical distribution of dust using ALMA Band 6 (1.3 mm) continuum emission and found that there are two distributions of dust with different scale heights of 5.1 and 15.7 au. For comparison, the scale height in our model is  $\sim 5$  au at a radius of 100 au. However, because our spatial resolution corresponds to roughly 19 au, larger than both of the scale heights from Matrà et al. 2019, the vertical structure is unresolved and thus has no effect on our results.

We calculate the dust temperature using the Monte Carlo Radiative Transfer code RADMC-3D (Dullemond et al. 2012) assuming a grain size of  $13.8 \mu\text{m}$ . We also calculate the temperature assuming large grains with a size of 1.38 mm and find that the dust temperature can differ by  $\sim 20\%$  at 100 au with respect to the small-grain case. However, this difference has little effect on the polarization fraction profile, which is the main focus of this paper that allows us to distinguish different grain-alignment mechanisms. The impact of the dust temperature on the intensity is compensated by a universal density scaling factor (see Section 6). The dust temperature also affects the timescales relevant for grain alignment, but the 20% difference is inconsequential (see Section 8). The gas and dust temperature distributions are plotted in the right panel of Figure 4.

Using the above values, we calculate the column density of dust for an edge-on view of the disk. We find that the column density peaks around 75 au at a value of  $8.2 \times 10^{-4} \text{ g cm}^{-2}$ . We thus find that the  $\beta$  Pic debris disk is very optically thin, unless the dust opacity is many orders of magnitude higher than  $1 \text{ cm}^2 \text{ g}^{-1}$ , which is unrealistic. The scattering optical depth is also expected to be much less than unity. We thus ignore scattering-induced dust polarization and consider only polarized thermal emission from aligned dust grains.<sup>21</sup>

The above information is sufficient to allow us to conduct radiative transfer calculations in Sections 5 and 6. Additional information about the strength of the magnetic and radiation fields is needed to analyze the alignment of dust grains, which we discuss in detail in Section 8.

#### 5. Constraints on the Intrinsic Dust Polarization Fraction

Here we present a simple semianalytical radiative transfer model whose parameter space we can explore quickly. The results have been checked against the Monte Carlo radiative transfer calculations that we present in Section 6 and show good agreement. In this model we assume an axisymmetric disk with the density and temperature profiles prescribed in Section 4.

##### 5.1. Dust Model

For simplicity and ease of computational cost, we assume small dust grains in the dipole regime. For the alignment of dust grains, we focus on the RAT mechanism. There are two possible configurations: grains are aligned either with the (radial) radiation flux ( $k$ -RAT) or with the magnetic field ( $B$ -RAT). Hereafter, we will sometimes refer to the radiation and magnetic fields as the “aligning fields.” When RAT is operating, the dust grains are aligned with their short axes along the aligning field and produce polarization perpendicular to it. As such, dust grains can be well represented by oblate spheroids (see, e.g., Yang et al. 2019). In the dipole regime, we assume that these small, oblate-spheroidal dust grains have polarizability  $\alpha_1$  and  $\alpha_3$  along the long and short axes of the dust grain, respectively (Bohren & Huffman 1983; Yang et al.

<sup>21</sup> This is further justified by our synthetic observations (see Section 6): when grain alignment is turned off, the scattering-induced polarization fraction is typically on the order of  $10^{-7}$ . We do not discuss this result further in this paper.

2016b). The absorption cross section of the dust grains is:

$$\sigma_{\text{abs}} = k \text{Im}[\alpha_1(1 + \cos^2 i) + \alpha_3 \sin^2 i] \quad (11)$$

and the polarization cross section is:

$\sigma_p = k \text{Im}[(\alpha_1 - \alpha_3)\sin^2 i]$ , (12)  
where  $i$  is the angle between the symmetry axis of the dust grain and the light propagation direction, and  $k = 2\pi/\lambda$  is the wavenumber. With this dust model, the polarization fraction at  $i = \pi/2$  is:

$$p_0 = \frac{\sigma_p}{\sigma_{\text{abs}}} = \frac{\text{Im}[\alpha_1 - \alpha_3]}{\text{Im}[\alpha_1 + \alpha_3]}. \quad (13)$$

We will refer to  $p_0$  as the ‘‘intrinsic polarization fraction,’’ which is the polarization fraction of the thermal dust emission when the dust grains are in an optically thin medium and are all uniformly viewed as edge-on by the observer. According to this model, the polarization fraction as a function of inclination angle is:

$$p(i) = \frac{\text{Im}[(\alpha_1 - \alpha_3)\sin^2 i]}{\text{Im}[\alpha_1(1 + \cos^2 i) + \alpha_3 \sin^2 i]} \\ = p_0 \sin^2 i + O(p_0^2). \quad (14)$$

Equation (14) shows that  $p_0$  and the geometric factor  $\sin^2 i$  can be separated completely to the leading order. As such, the observed polarization fraction scales approximately linearly with the intrinsic polarization fraction  $p_0$  for any given geometry of the aligning fields along the line of sight.

The observed polarization depends not only on  $p_0$ , but also on the geometry of the underlying aligning field along the line of sight and on the degree of grain alignment. The geometric effect will be modeled later. Here we discuss the observable effect of the degree of grain alignment. If the dust grains are perfectly aligned, the polarization profile is well described by Equation (14). If the dust grains are poorly aligned, the polarization profile will also follow Equation (14), except that  $p_0$  will be replaced with  $Rp_0$ , where  $R$  is the so-called ‘‘Rayleigh reduction factor’’ (Lee & Draine 1985):

$$R = \frac{3}{2} \left( \langle \cos^2 \eta \rangle - \frac{1}{3} \right), \quad (15)$$

where  $\langle \cos^2 \eta \rangle$  is averaged over the ensemble of dust grains, with  $\eta$  being the angle between the symmetry axis of dust grains and the alignment axis. For perfectly aligned grains,  $\langle \cos^2 \eta \rangle = 1$  and  $R = 1$ . For nonaligned grains,  $\langle \cos^2 \eta \rangle = 1/3$  and  $R = 0$ . Because  $R$  and  $p_0$  are always multiplied by one another, we cannot tell them apart observationally. In the following radiative transfer calculations and in Section 6, we will assume  $R = 1$  and take the intrinsic polarization fraction  $p_0$  as the single parameter describing our dust grains.

## 5.2. Polarization Profiles for k-RAT and B-RAT

In the  $k$ -RAT regime, the dust grains are aligned with their short axes along the direction of the radiation flux. Given our prescribed axisymmetric model, the radiation flux can only be in the radial direction. The dust grains aligned with such a radiation field are thus oriented with their short axes along the radial direction. For a dust grain placed in the debris disk with azimuth angle  $\theta$ , the angle between the line of sight and the

symmetry axis of the dust grain is  $i = \pi/2 - \theta$ . The Stokes  $I$  (total intensity) dust emission from  $k$ -RAT,  $I_k$ , can then be calculated as:

$$I_k \propto \int_{-\infty}^{\infty} \rho(r(x, l))T(r(x, l)) \\ \times [\omega(1 + \sin^2 \theta(x, l)) + \cos^2 \theta(x, l)] dl, \quad (16)$$

where  $\rho(r)$  is the density profile and  $T(r)$  is the temperature profile.  $r(x, l) = \sqrt{x^2 + l^2}$  and  $\theta(x, l) = \tan^{-1}(l/x)$  are the distance from the center and the azimuthal angle in the disk, respectively, where  $x$  is the location of the line of sight in the sky plane and  $l$  is the distance along the line of sight ( $l = 0$  lies along the  $x$ -axis).  $\omega \equiv \text{Im}[\alpha_3]/\text{Im}[\alpha_1]$  is the ratio of the absorption cross sections along the two principle axes, which is related to the intrinsic polarization fraction as  $\omega = (1 + p_0)/(1 - p_0)$ . We illustrate the geometry of our setting in Figure 5, where the red oval represents a grain aligned via the  $k$ -RAT mechanism.

We define the Stokes parameters in our models such that  $Q > 0$  implies polarization along the  $z$  axis (see Figure 5), i.e., the direction perpendicular to the plane of the debris disk:

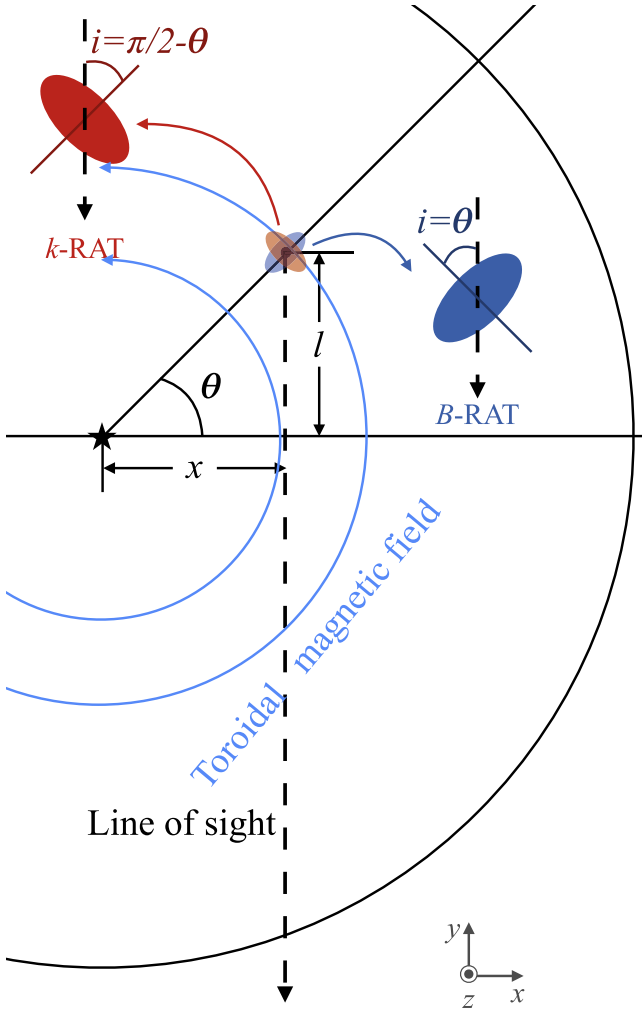
$$Q_k \propto \int_{-\infty}^{\infty} \rho(r(x, l))T(r(x, l)) \\ \times (\omega - 1)\cos^2 \theta(x, l) dl. \quad (17)$$

This definition of  $Q$  in our models is analogous to our definition of  $Q'$  in the transformed reference frame discussed in Section 3.1.

For simplicity, in the  $B$ -RAT regime we assume a purely toroidal magnetic field. A toroidal field configuration is a natural outcome in both a rotating disk and in the outer reaches ( $\sim 50$ – $100$  au in the case of the Sun) of the stellar-dominated heliosphere of a rotating star (Owens & Forsyth 2013), and thus should be the magnetic field configuration near the disk midplane where most dust grains reside. While observations of protoplanetary disks suggest that some may have significant poloidal components of their magnetic fields (Li et al. 2016; Alves et al. 2018), a predominantly poloidal magnetic field in  $\beta$  Pic would produce polarization along the major axis of the debris disk, which is perpendicular to the full-disk-averaged polarization orientation that we observe. Thus, if  $B$ -RAT is the cause of the polarization signal, poloidal magnetic fields are most likely playing a subdominant role in the  $\beta$  Pic system.<sup>22</sup> In this regime, dust grains are aligned with their short axes along the magnetic field direction, with the symmetry axis of the oblate dust grain making an angle of  $i = \theta$  with the line of sight. We represent the grain aligned via  $B$ -RAT as a blue oval in Figure 5. The Stokes  $I$  emission from  $B$ -RAT,  $I_B$ , can then be calculated as:

$$I_B \propto \int_{-\infty}^{\infty} \rho(r(x, l))T(r(x, l)) \\ \times [a(1 + \cos^2 \theta(x, l)) + \sin^2 \theta(x, l)] dl. \quad (18)$$

<sup>22</sup> Note that we cannot rule out poloidal magnetic fields completely here. While small grains aligned with poloidal magnetic fields will produce polarization along the major axis of the disk, which is the opposite of what we see, larger grains that are aligned via  $B$ -RAT can experience the effect of polarization reversal, or ‘‘negative polarization’’ (see, e.g., Guillet et al. 2020), which produces polarization along the magnetic field direction instead of perpendicular to it. Such complications are left for future studies.

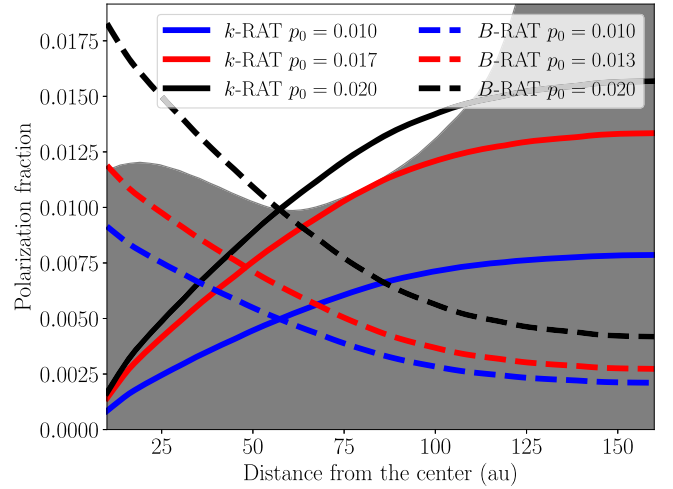


**Figure 5.** The setting of our semianalytical radiative transfer model. The black arc represents the  $\beta$  Pic debris disk. The horizontal line is the sky plane, which is perpendicular to our line of sight, shown as a dashed arrow. A representative dust grain (black dot) has an azimuth angle  $\theta$  measured counterclockwise from the sky plane.  $x$  is the distance from the line of sight to the center of the disk.  $l$  is the distance along the line of sight, with  $l = 0$  being in the plane of the sky. We consider two alignment mechanisms. For  $k$ -RAT, we have a dust grain (red oval) whose short axis is aligned with the radial radiation flux, which thus makes an angle  $i = \pi/2 - \theta$  with the line of sight. For  $B$ -RAT, we have a dust grain (blue oval) whose short axis is aligned with a toroidal magnetic field such that the symmetry axis of the dust grain makes an angle  $i = \theta$  with the line of sight.

With the same definition of Stokes  $Q$ , we have:

$$Q_B \propto \int_{-\infty}^{\infty} \rho(r(x, l)) T(r(x, l)) \times (\omega - 1) \sin^2 \theta(x, l) dl. \quad (19)$$

We can now calculate the polarization fraction as a function of  $x$ , the distance from the center of the disk, for grains aligned via both the  $k$ -RAT and  $B$ -RAT mechanisms. We plot the results in Figure 6. While both  $k$ -RAT and  $B$ -RAT predict polarization angles aligned with the minor axis of the disk, they have different polarized intensity profiles as a function of distance along the major axis. We can see that for  $k$ -RAT (solid curves), polarization increases toward larger radii. The strongest constraint on our  $k$ -RAT models comes from the nondetection between 70 and 100 au in the folded ALMA data (see the right panel of Figure 3), which allows us to exclude



**Figure 6.** Polarization fraction as a function of distance from the center of our modeled debris disk. Solid lines show results for  $k$ -RAT alignment. Dashed lines show results for  $B$ -RAT alignment. Different colors represent dust grains with different values of the intrinsic polarization fraction  $p_0$ . The shaded region is the region permitted by our ALMA observations; the upper envelope of the region is the same as the curve shown in the right-hand panel of Figure 3.

models with intrinsic polarization fractions  $p_0 \gtrsim 1.7\%$ . On the other hand, if we assume  $B$ -RAT (dotted curves), the polarization decreases toward larger radii. The strongest constraint on our  $B$ -RAT models comes from the observational upper limits toward the center of the disk, where we expect a large amount of polarization. In this case, we can put a slightly stronger constraint on the intrinsic polarization fraction, excluding models with  $p_0 \gtrsim 1.3\%$ .

We can see that the difference in polarization profile is the key to distinguishing between  $k$ -RAT and  $B$ -RAT. These different profiles are the result of the geometry of dust grains (as viewed by the observer) that have been aligned with respect to the different aligning fields: the radiation field in the case of  $k$ -RAT, and the magnetic field in the case of  $B$ -RAT. For  $k$ -RAT ( $B$ -RAT), dust grains are aligned with radial (toroidal) fields, which are parallel (perpendicular) to the line of sight near the center of the disk and perpendicular (parallel) to the line of sight toward the edges of the disk. Hence, dust grains aligned via  $k$ -RAT ( $B$ -RAT) are viewed by the observer to be face-on (edge-on) near the center, and edge-on (face-on) toward the edges of the disk. Because an edge-on dust grain emits more polarized light and because the light from face-on grains is essentially unpolarized (see Equation (14)),  $k$ -RAT ( $B$ -RAT) predicts larger polarization toward the edges (center) of the disk. In the next section, we will perform 3D radiative transfer simulations and use this difference in the polarization profiles to identify the underlying grain-alignment mechanism in  $\beta$  Pic.

## 6. Synthetic Observations

Here we use RADMC-3D to perform a synthetic observation that fits our observation well. We set up a disk model in spherical polar coordinates and assume small dust grains with a single size  $a = 13.8 \mu\text{m}$ ,<sup>23</sup> which corresponds to a size

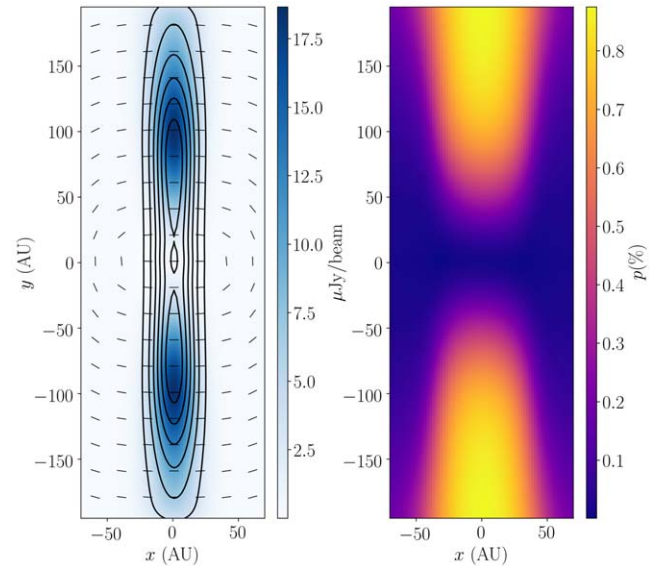
<sup>23</sup> It is possible for dust grains to have a distribution of different sizes; however, having a range of different (small) grain sizes does not impact the polarization profile. Furthermore, the effect of multiple grain sizes on the opacity is compensated for by the universal scaling factor for dust density.

parameter  $x = 0.1$ . We assume small dust grains in the dipole regime for their well behaved phase function (i.e., the grains' [polarized] cross section as a function of scattering angle) and ease of computational effort. Larger dust grains show very complicated phase functions, and the calculation of their optical properties is much more costly; we leave the exploration of models with large dust grains for later work. To compensate for the effects of different dust opacities, we allow the dust density to scale by the same factor across the whole domain in order to achieve the correct intensity. The optical properties for small dust grains in the dipole regime depend both on the composition of dust grains and on the aspect ratio of the oblate spheroids. However, in the end, only the intrinsic polarization fraction  $p_0$  matters. We thus choose to fix the composition of dust grains and to vary only the aspect ratio  $s$ . We adopt the dust model from Birnstiel et al. (2018), which is a mixture of 20% water ice (Warren & Brandt 2008), 33% astronomical silicates (Draine 2003), 7% troilite (Henning & Stognienko 1996), and 40% refractory organics (Henning & Stognienko 1996) by mass. Note that this dust model is designed for dust in protoplanetary disks, not for a debris disk like  $\beta$  Pic. However, the choice of dust composition does not affect the polarization profile, which is the main focus of this paper.

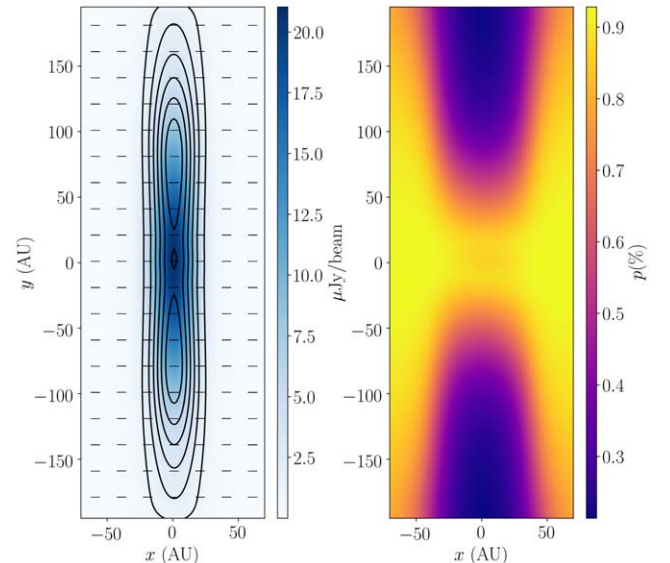
We first calculate the dust temperature assuming spherical dust grains (this temperature is also used in Section 5). We calculate the optical properties of the dust grains assuming perfect alignment and an oblate-spheroidal geometry with an aspect ratio  $s$ . We then calculate the full Stokes parameters assuming oblate grains aligned via the  $k$ -RAT mechanism, i.e., with the short axes of the dust grains aligned in the radial direction. We then smooth image with using the  $\sim 1''$  synthesized beam from the ALMA observations. Since the observed averaged polarization fraction depends roughly linearly on the intrinsic polarization fraction (see Equation (14)), and thus depends monotonically on the aspect ratio  $s$ , we can easily obtain the best model through a simple binary search in the parameter space of  $s$ . We do so with a minimum change in  $s$  of 0.0001.

In Figure 7, we show the best-fit synthetic observation assuming  $k$ -RAT, which has a dust aspect ratio of  $s = 1.0171$  and an intrinsic polarization fraction  $p_0 = 1.2\%$ . Averaging the Stokes parameters from this synthetic observation yields an averaged polarization fraction of 0.50%, which matches our full-disk-averaged observations very well. For comparison, we conduct the same calculation assuming  $B$ -RAT, i.e., where grains are aligned with their short axes along the toroidal direction. In Figure 8, we show the best-fit  $B$ -RAT model, which has  $s = 1.0125$  and  $p_0 = 0.90\%$ , and yields an averaged polarization fraction of 0.51%. We can clearly see the difference between these two models: the  $k$ -RAT model has two off-center peaks of polarization, whereas the polarization in the  $B$ -RAT model is concentrated near the center of the disk.

To compare these two models in more detail, in Figure 9, we plot total intensity and polarized intensity cuts along the disk midplane for both the data and the models. The blue and orange curves represent results from the  $B$ -RAT and  $k$ -RAT models, respectively. We use solid lines to show total intensity profiles and dashed lines to represent polarized intensity  $Q$  (note that  $U = 0$  due to the symmetry of the system). We multiply the total intensity by 0.02 to show both the polarized and unpolarized intensities clearly on the same scale. We also plot



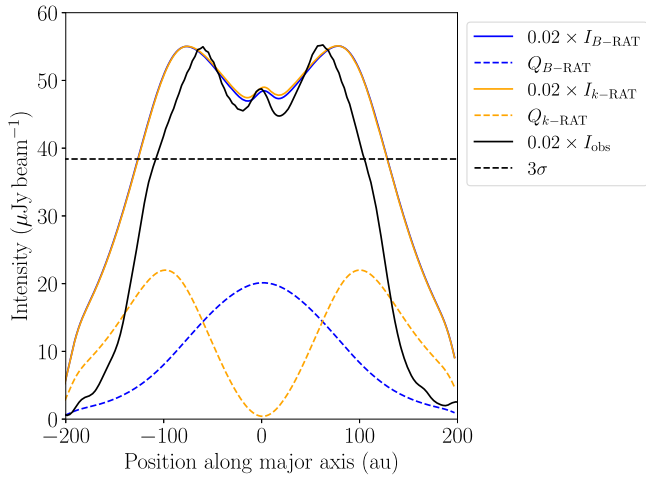
**Figure 7.** A synthetic observation assuming grains aligned via  $k$ -RAT. The grain size is  $13.8 \mu\text{m}$ , which corresponds to a size parameter of  $x = 0.1$ . Left: contours are total intensity. Color scale is polarized intensity in  $\mu\text{Jy beam}^{-1}$ . The line segments are of the same length and represent the polarization orientation. Right: the color scale represents the polarization fraction.



**Figure 8.** Same as Figure 7 but for  $B$ -RAT.

our observed total intensity as a black curve, along with a straight black dashed curve showing the  $3\sigma$  upper limit in the debiased polarized intensity  $P$ , where  $\sigma = 12.8 \mu\text{Jy beam}^{-1}$ . We can see that both models predict polarized intensity levels below the noise level in the resolved map. They also yield full-disk-averaged polarization fractions similar to our detected value (0.51%). Hence, we cannot distinguish the two models using only the full-disk-averaged value of the polarization fraction from our observations.

To distinguish between  $k$ -RAT and  $B$ -RAT, we use three boxes that covers the NE third, center third, and the SW third of the disk separately (see Section 3.2 for a description of the averaging box). All boxes have a width along the minor axis of  $1''.7$ , or  $32.7 \text{ au}$ , the same as the full-disk averaging box. The



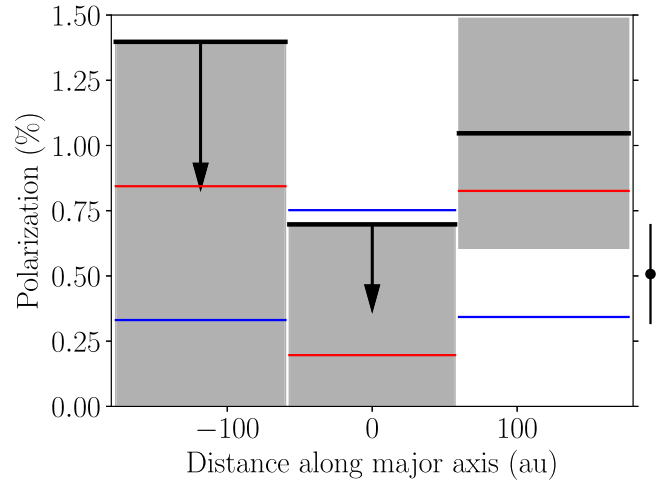
**Figure 9.** Cuts along the major axis of the modeled and observed disk of  $\beta$  Pic. Blue, orange, and black curves represent the  $B$ -RAT model,  $k$ -RAT model, and our observations, respectively. Solid lines represent the total intensity, while the dashed lines represent the polarized intensity. To represent the polarized intensity from the ALMA observations, we plot a  $3\sigma$  upper limit as a dashed line, where  $\sigma=12.8 \mu\text{Jy beam}^{-1}$  is the rms noise level in the debiased  $P$  map.

polarization fraction values from our ALMA observations and from the two synthetic observations, measured in each of the three averaging boxes, are shown in Figure 10. We see that  $B$ -RAT can be excluded, because it predicts too much polarization in the center box, larger than the  $3\sigma$  upper limit in that box. It also predicts polarization that is too weak in the SW box; the value from the model is more than  $1\sigma$  lower than the marginal detection ( $S/N=2.4$ ) of  $P$  in the ALMA data reported in Section 3.2. On the other hand, while the  $k$ -RAT model fails to predict the asymmetry between the NE and SW thirds, the model otherwise agrees very well with the observations: the predicted  $k$ -RAT polarization in the NE and central boxes lies below  $3\sigma$  upper limits from the observations, and the polarization in the SW third is within  $\pm 1\sigma$  of our tentative detection. In short, *We find that  $k$ -RAT is the likely mechanism producing the polarized emission in  $\beta$  Pic.*

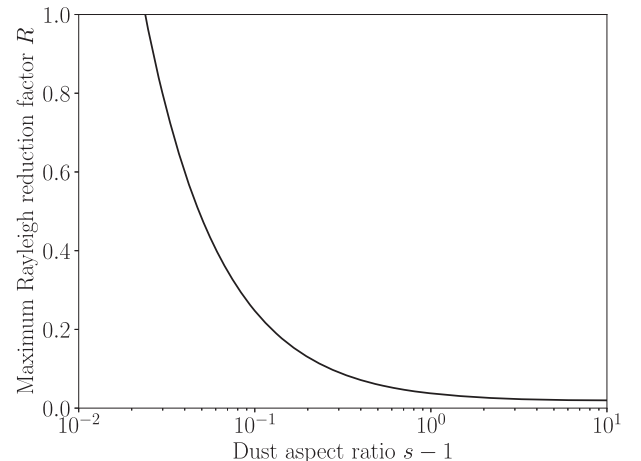
## 7. Constraints on Dust Models

In Section 5, we derive constraints on the intrinsic polarization fraction  $p_0$  of the dust grains. We find that  $p_0$  must be  $<1.7\%$  in order to explain our nondetection in the spatially resolved map. While  $p_0$  is directly connected to the observed polarization, which scales approximately linearly with  $p_0$ , it is not directly connected to the dust models. In this section we discuss constraints on our dust models, regarding both the geometry of the grains and the degree of grain alignment. The dependence of  $p_0$  on the dust composition is complex and is expected to be secondary to the dependence of  $p_0$  on the dust aspect ratio  $s$ . Consequently, we fix our dust composition and adopt the dust model from Birnstiel et al. (2018), as before.

We first calculate the intrinsic polarization fraction  $p_0$  as a function of the aspect ratio  $s$  for perfectly aligned, small, oblate-spheroidal dust grains. Since the product of the Rayleigh reduction factor and the intrinsic polarization fraction  $Rp_0$  is what determines the observed polarization fraction (see discussion in Section 5), we can divide the upper limit of  $1.7\%$  by  $p_0$  to get an upper limit for the Rayleigh reduction factor  $R$ . We plot the results in Figure 11.



**Figure 10.** Box-averaged polarization fractions with errors. The  $x$ -axis ranges from the NE (negative) to the SW (positive); the width of the three bands represents the coverage of each box along the major axis of the disk. The red and blue lines show the box-averaged polarization fractions in the  $k$ -RAT and  $B$ -RAT models, respectively. We treat the observational results, which we plot as thick black lines, in two different ways. For the NE and central thirds, we plot the  $3\sigma$  upper limits with downward-pointing arrows. For the SW third, where we have a marginal detection of polarized dust emission, we plot our detected polarization fraction, surrounded by a gray box showing  $\pm 1\sigma$  error. Just to the right of the plot we show a dot with  $\pm 1\sigma$  error bars representing the averaged polarization fraction in the whole disk ( $0.51\% \pm 0.19\%$ ).



**Figure 11.** The constraint on the Rayleigh reduction factor ( $Rp_0 < 1.7\%$ ) as a function of aspect ratio  $s$  for small, oblate-spheroidal dust grains. See text for details.

We can see that grains with aspect ratio  $s < 1.025$  can be perfectly aligned with  $R=1$  while producing polarization below our detection limit in the resolved map. However, those aspect ratios are close to unity (i.e., grains that are nearly round), which is unreasonable. For comparison, the disk of Saturn has an aspect ratio of approximately 1.1 (Gehrels et al. 1980) and a sample of asteroids imaged by Gaia have an average aspect ratio of 1.25 (Mommert et al. 2018). It is hard to imagine dust grains having such small aspect ratios after collisional fragmentation; and indeed, interplanetary dust particles from our Solar system, which should be similar to the dust grains in  $\beta$  Pic, show visibly noncircular aspect ratios (Bradley 2003). For more realistic dust grains with larger aspect ratios, perfect alignment models are rejected. In order for their polarized emission to remain undetected, these more elongated dust grains would need to be aligned with low grain-

alignment efficiency. The maximum permitted  $R$  drops quickly as we increase  $s$ . For example, when  $s = 1.1$ , we have  $R < 0.2$ , indicating low alignment efficiency. In the limit of  $s \gg 1$ , the intrinsic polarization fraction  $p_0 = 1$ , corresponding to an upper limit of  $R < 0.017$ . We will discuss this result in the context of grain alignment theory in Section 8.

One caveat of the above discussion is that we assume compact dust grains. Li & Greenberg (1998) modeled the  $\beta$  Pic disk with a comet dust model and found that the dust grains are highly porous, with a porosity of around 0.95. The intrinsic polarization of porous dust grains was recently studied by Kirchschrager et al. (2019), who found that  $p_0$  can be reduced by about a factor of 5 for dust grains with a porosity of 0.8. Our aforementioned constraints on the degree of alignment  $R$  can be loosened by the same factor. For example, if we have dust grains with an aspect ratio  $s = 1.5$  and a porosity of 0.8, the degree of alignment  $R < 0.3$ , whereas compact dust grains with  $s = 1.5$  have  $R < 0.06$ .

Another major caveat is the assumption of small grains. Cho & Lazarian (2007) showed that the intrinsic polarization fraction is very low for large grains. It is also possible that the alignment degree of very large grains ( $>1$  mm) is different from (and very small compared with) the alignment degree of small grains. In both cases, large grains do not contribute polarized emission, but still contribute to the total intensity (Stokes  $I$ ) emission. It is possible that there are well aligned small grains alongside large dust grains in  $\beta$  Pic, and thus the aforementioned constraint on the alignment degree of the small grains would be less stringent (i.e., the degree of alignment could be higher than our estimate shown in Figure 11). We leave detailed explorations of models with large dust grains for future studies.

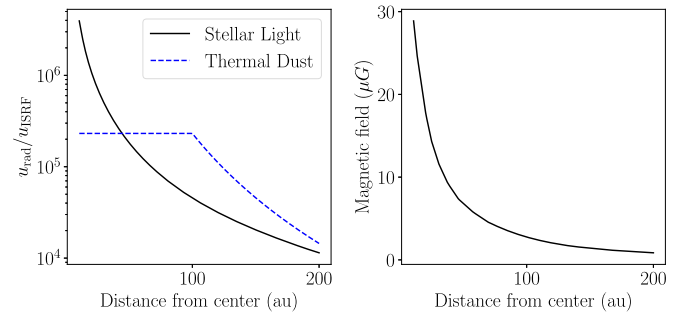
## 8. Dust-grain Alignment Analysis

### 8.1. Models for the Magnetic Field and the Radiation Field

The energy density and anisotropy of the radiation field are important for the theory of dust-grain alignment via the RAT mechanism, which is currently the favored mechanism for grain alignment. There are three major contributions to the radiation energy density: thermal emission from dust, the cosmic microwave background (CMB), and stellar illumination. Kral et al. (2017) calculated the far-infrared energy density in the radiation field of the  $\beta$  Pic debris disk and found that the energy density of thermal dust emission is greater than that of the CMB. We consequently ignore the CMB in this work. The thermal dust emission peaks around  $50 \mu\text{m}$  and has a total energy density of  $\nu F_\nu \approx 2 \times 10^{-7} \text{ erg cm}^{-3}$ . The energy density distribution is relatively flat within the inner 100 au of the disk and falls off at larger radii roughly as  $r^{-4}$ . The anisotropy of the radiation field  $\gamma$  from thermal dust emission is typically on the order of 0.1 (Tazaki et al. 2017); we use this value in our analysis.

Close to the central star  $\beta$  Pic, the stellar illumination is much stronger than the dust thermal emission. For a central star with a bolometric luminosity  $L = 8.7L_\odot$ , the radiation energy density is:

$$u = \frac{L}{4\pi r^2 c} = 3.95 \times 10^{-4} r_{\text{au}}^{-2} \text{ erg cm}^{-3}, \quad (20)$$



**Figure 12.** Left: The energy density profiles of the stellar radiation and thermal dust emission. Right: The magnetic field-strength profile assumed in our grain alignment analysis.

where  $r$  is the distance from the central star and  $r_{\text{au}}$  is the distance in au. The stellar illumination is purely radial. We assume that the anisotropy of the radiation field for this component is  $\gamma = 1$ . The energy-weighted average wavelength, defined as  $\bar{\lambda} \equiv \int u_\lambda \lambda d\lambda / \int u_\lambda d\lambda$ , is  $\bar{\lambda} = 0.66 \mu\text{m}$  for an effective temperature of 8052 K. We plot the energy density profiles for both the stellar radiation and the thermal dust emission in the left panel of Figure 12.

Regarding the magnetic field strength, Kral & Latter (2016) argue that nonideal MHD effects are subdominant in the  $\beta$  Pic debris disk and that the MRI is likely to be operating in the disk. It is well known that the MRI is suppressed if the magnetic field is too strong, i.e., when the plasma  $\beta \lesssim 10$ , where  $\beta$  is defined as the ratio of thermal pressure to magnetic pressure (e.g., Davis et al. 2010). For simplicity, we adopt a magnetic field model assuming  $\beta = 10$  everywhere. We plot the resulting profile of the magnetic field strength in the right-hand panel of Figure 12. The field strength of our model at a radius of 50 au is approximately  $5 \mu\text{G}$ , which is similar both to the strength of the interplanetary magnetic field measured by Voyager 1 and 2 at a similar distance from our Sun (Burlaga et al. 2003) and to the  $6 \mu\text{G}$  strength of the magnetic field in the cold neutral interstellar medium of the Milky Way (Heiles & Troland 2005).

### 8.2. Alignment Timescales

The alignment of dust grains is a complicated process. We first compare several timescales involved in the grain-alignment process following the work presented in Tazaki et al. (2017) and Yang (2021). Three of the most important timescales are the gas damping timescale, the Larmor precession timescale, and the RAT precession timescale.

The gas damping timescale is the timescale on which random bombardment by gas particles misaligns the dust grains. In our disk model the gas component is assumed to be a mixture of carbon and oxygen atoms (or their ions; electrons are ignored in the damping process). The mean molecular weight is 14, as opposed to the usual 2.34 for protoplanetary disks dominated by molecular hydrogen. The gas damping timescale  $t_g$  is as follows:

$$t_g = 2.3 \times 10^6 \text{ yr} \times \hat{\rho}_s \left( \frac{a}{5 \mu\text{m}} \right) \times \left( \frac{n_g}{20 \text{ cm}^{-3}} \right)^{-1} \left( \frac{T_g}{85 \text{ K}} \right)^{-1/2}, \quad (21)$$

where  $\hat{\rho}_s = \rho_s / (3g \text{ cm}^{-3})$  is the reduced solid density of the dust grain, which we take as  $\hat{\rho}_s = 1$ ;  $a$  is the effective radius of the dust grain;  $n_g$  is the number density of gas particles; and  $T_g$  is the gas temperature.

As a result of the Barnett effect, a rotating dust grain has a magnetic moment proportional to its angular momentum (Barnett 1915). Hence, there is a Larmor precession timescale  $t_L$  defined as the precession period of dust grains around an external magnetic field:

$$t_L = 2.1 \times 10^2 \text{ yr} \times \hat{\chi}^{-1} \hat{\rho}_s \left( \frac{T_d}{15 \text{ K}} \right) \times \left( \frac{B}{5 \mu\text{G}} \right)^{-1} \left( \frac{a}{5 \mu\text{m}} \right)^2, \quad (22)$$

where  $T_d$  is the dust temperature,  $B$  is the magnetic field strength, and  $\chi = 10^{-3} \hat{\chi} (T_d / 15 \text{ K})^{-1}$  is the magnetic susceptibility of the dust grain; for regular paramagnetic materials,  $\hat{\chi} \approx 1$ . If dust grains contain clusters of ferromagnetic material, known as “superparamagnetic inclusions,”  $\chi$  can be enhanced by up to a factor of  $10^3$  (Jones & Spitzer 1967; Yang 2021).

The third timescale is the RAT precession timescale. Radiation can exert torques (i.e., RATs) on dust grains that have a significant helicity. The RAT precession timescale  $t_{\text{rad,p}}$  is the precession period of the dust grains experiencing such torques:

$$t_{\text{rad,p}} = 4 \times 10^{-3} \text{ yr} \times \hat{\rho}_s^{1/2} \hat{s}^{-1/3} \left( \frac{a}{5 \mu\text{m}} \right)^{1/2} \left( \frac{T_d}{15 \text{ K}} \right)^{1/2} \times \left( \frac{u_{\text{rad}}}{2 \times 10^5 u_{\text{ISRF}}} \right)^{-1} \left( \frac{\bar{\lambda}}{0.66 \mu\text{m}} \right)^{-1} \left( \frac{\gamma |\overline{Q}_T|}{0.04} \right)^{-1}, \quad (23)$$

where the radiation field energy density  $u_{\text{rad}}$  is normalized by  $u_{\text{ISRF}} = 8.64 \times 10^{-13} \text{ erg cm}^{-3}$ , the energy density of the standard interstellar radiation field (ISRF; Mathis et al. 1983; Lazarian & Hoang 2007a).  $|\overline{Q}_T|$  is a dimensionless parameter describing the strength of the torque that follows the following piecewise function (Lazarian & Hoang 2007a):

$$|\overline{Q}_T| \approx \begin{cases} 2.3 \left( \frac{\lambda}{a} \right)^{-3} & \text{for } \lambda > 1.8 a \\ 0.4 & \text{for } \lambda \leq 1.8 a \end{cases}. \quad (24)$$

Since we have both stellar illumination and thermal dust emission, we calculate the RAT precession timescale for these two components separately according to Equation (23), and then take the harmonic average of these two results to obtain the RAT precession timescale when both sources are in action.

Although other grain-alignment mechanisms exist, we focus only on the RAT alignment theory. Grain alignment via the Gold mechanism (Gold 1952) and Mechanical Alignment Torques (MATs; Lazarian & Hoang 2007b) both rely on differential motion between the gas and the dust to operate; both of these mechanisms should be less effective than RATs at aligning grains in the  $\beta$ Pic debris disk because of the low density of gas particles and correspondingly rare interactions between gas and dust, as shown in Equation (21).

In debris disks, the timescale of collisions between dust grains is important because it determines the lifetime of dust

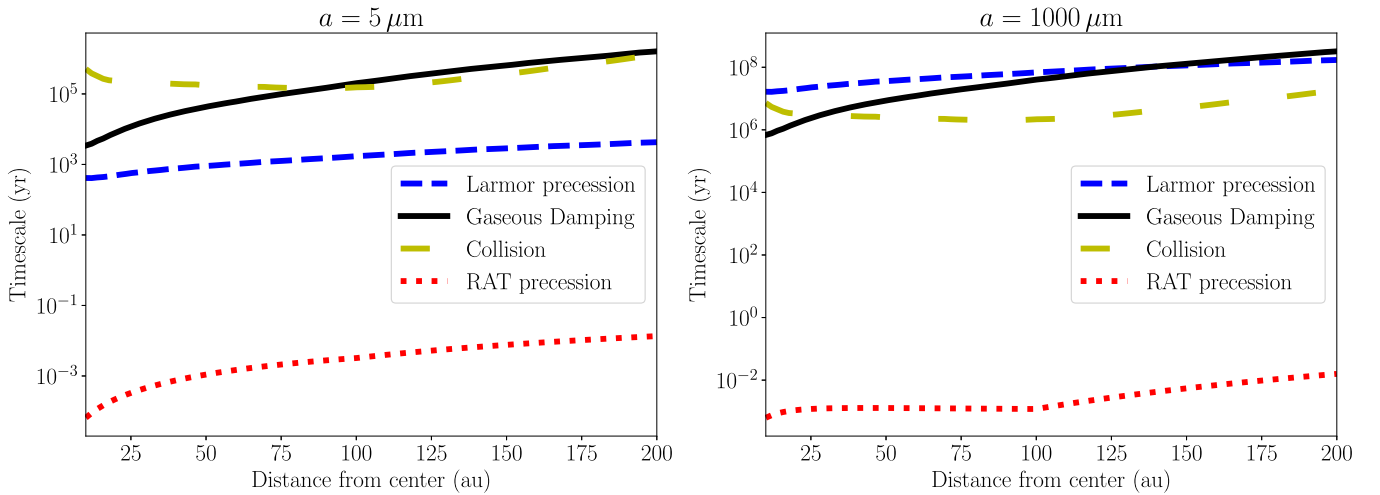
grains (i.e., how long they survive before being collisionally destroyed). If we assume the dust grains are primarily destroyed by collisions with similar sized grains, and we further assume that the dust grains have a power law size distribution  $dn/da \sim a^{-3.5}$  with a maximum grain size of  $a_2 = 1 \text{ cm}$  (Zagorovsky et al. 2010), we can derive the collision timescale using Equation (11) of Ahmic et al. (2009) as follows:

$$t_{\text{col}} = \frac{5P\rho_s\sqrt{aa_2}}{54\Sigma}, \quad (25)$$

where  $P$  is the local Keplerian rotation period and  $\Sigma$  is the dust column density (viewed face-on).

In Figure 13, we show a comparison of the four timescales  $t_g$ ,  $t_L$ ,  $t_{\text{rad,p}}$ , and  $t_{\text{col}}$  as a function of distance from the center of the  $\beta$  Pic debris disk. In the left panel we show the results for small dust grains with  $a = 5 \mu\text{m}$ , which is close to the blow-out size of dust grains in  $\beta$  Pic (Burns et al. 1979; Arnold et al. 2019). We see that the Larmor precession timescale is always smaller than the gas damping timescale for small grains. In addition, we find that RAT precession is at least four orders smaller than the other two timescales, and thus RAT is very likely to be operating. In the right panel, we show the results for large dust grains with  $a = 1 \text{ mm}$ . We see that the Larmor precession and gas damping timescales are comparable to one another, especially at the location of the dusty ring at  $\sim 100 \text{ au}$ . Note that this applies only to regular paramagnetic grains. If we consider superparamagnetic inclusions, the Larmor precession timescale can easily be reduced by a factor of  $\sim 10^{2-3}$ , which would result in a Larmor precession timescale that is always smaller than the gas damping timescale. In summary, while  $t_g$  and  $t_L$  can be comparable depending on the grain size we consider, the RAT precession timescale is 4–10 orders of magnitude smaller than both of them. There is thus no doubt that the RAT alignment mechanism is operating in this system. We also find that the collision timescale  $t_{\text{col}}$  is smaller than both  $t_L$  and  $t_g$  for 1 mm dust grains, which means such dust grains would be destroyed through collisions before they can be aligned with magnetic fields.

When RAT is operating, there are two possible outcomes. In the presence of a strong external magnetic field, dust grains will become aligned with the magnetic field (the  $B$ -RAT case). In the absence of a strong external magnetic field, dust grains will still be aligned, but now with respect to the radiation flux instead of with respect to the magnetic field (the  $k$ -RAT case). The strength of the magnetic field is quantified by the Larmor precession timescale  $t_L$ . As suggested by Lazarian & Hoang (2007a) and Tazaki et al. (2017), in the regime where  $t_{\text{rad,p}} \ll t_L$ , we should have  $k$ -RAT alignment instead of  $B$ -RAT alignment. And indeed, in order for  $B$ -RAT to dominate over  $k$ -RAT in  $\beta$  Pic at a distance of, e.g., 100 au, the strength of the magnetic field would need to be  $\sim 1.5 \text{ mG}$  for  $5 \mu\text{m}$ -sized dust grains and  $\sim 160 \text{ G}$  for 1 mm grains, in both cases considering grains with superparamagnetic inclusions with  $\hat{\chi} = 10^3$  (Yang 2021). Given the microgauss-level magnetic field strengths discussed in Section 8.1, these high values for the magnetic field in  $\beta$  Pic are unrealistic. In summary,  $k$ -RAT is the likely mechanism producing the polarization we see in  $\beta$  Pic. This is in agreement with the analysis of both our ALMA observations and our synthetic observations.



**Figure 13.** Comparison of dust-grain alignment timescales for small dust grains ( $a = 5 \mu\text{m}$ , left panel) and large dust grains ( $a = 1 \text{ mm}$ , right panel).

### 8.3. Degree of Alignment

Even though the above timescale comparisons show that RAT is operating very well, it does not guarantee perfect alignment of dust grains with respect to the magnetic or radiation field. There are several other factors that come into play to determine the degree of alignment, which equals the Rayleigh reduction factor  $R$ .

The main one is the internal alignment, i.e., the alignment of the dust grain’s angular momentum  $J$  with the grain’s principle axis of maximum inertia. Tazaki et al. (2017) considered several relevant relaxation processes including Barnett relaxation of both electrons and nuclei, Barnett relaxation with superparamagnetic inclusions, and inelastic dissipation. The results are shown in their Figure 2. For grains larger than  $5 \mu\text{m}$ , the internal relaxation timescale,  $t_{\text{int}}$ , is longer than  $\sim 3 \times 10^6 \text{ yr}$ . The internal relaxation timescale increases rapidly as grain size  $a$  increases (increasing roughly as  $a^7$ ). We can thus conclude that the internal relaxation timescale is much longer than the other relevant timescales in the entire  $\beta \text{ Pic}$  debris disk, and thus grains are not internally aligned.

Without internal alignment, grain alignment is still possible, as shown by Hoang & Lazarian (2009). This is especially true when there are so-called “high- $J$  attractors,” which are attracting stationary points in the phase diagram (whose axes are the angle with the aligning field  $\theta$  and the angular momentum  $J$ ; see, e.g., Lazarian & Hoang 2007a) where grains have suprathermally rotating angular momentum. Grains at high- $J$  attractors are expected to be aligned perfectly, regardless of internal relaxation (Hoang & Lazarian 2009). Grains at low- $J$  attractors are subject to thermal fluctuations, and can also be aligned in the “wrong” configuration, i.e., with their short axes not along the direction of the aligning field; in this case the degree of alignment is strongly affected by the lack of internal relaxation (Hoang & Lazarian 2009). Whether high- $J$  attractors exist depends on the geometry, composition, and size of the dust grains.

Let  $f_{\text{high-}J}$  be the fraction of dust grains aligned at high- $J$  attractor points. The timescale comparison in Section 8.2 shows that we are in a regime where  $t_{\text{rad,p}} < t_g < t_{\text{int}}$ . For grains aligned at high- $J$  attractors, we have perfect alignment. For grains not aligned at high- $J$  attractors, the degree of alignment is 0 due to the lack of internal alignment (Hoang & Lazarian 2009; see also discussions by Tazaki et al. 2017).

As a result,  $R = f_{\text{high-}J}$ . From our previous constraint on the Rayleigh reduction factor (see Section 7 and Figure 11) we conclude that the  $f_{\text{high-}J}$  is likely to be very small. For dust grains with aspect ratios  $s > 1.1$ , we have  $f_{\text{high-}J} < 0.2$ . For grains with  $s > 2$ , we have  $f_{\text{high-}J} < 0.037$ . These values of  $f_{\text{high-}J}$  are far smaller than the values typically adopted in the literature. Recently, Herranen et al. (2021) studied the alignment efficiency of ensembles of Gaussian random ellipsoidal dust grains and found that the alignment efficiency of small grains exposed to the ISRF can reach levels as high as  $\sim 0.5$ . Additionally, Le Gouellec et al. (2020) found evidence for high grain-alignment efficiency in Class 0 protostellar cores. Whether our inference of low grain-alignment efficiency in  $\beta \text{ Pic}$  is possible with realistic distributions of dust grains is a question for RAT theory to answer.

## 9. Conclusions

We present  $870 \mu\text{m}$  ALMA polarization observations of thermal dust emission toward the edge-on  $\beta \text{ Pic}$  debris disk. Our analysis of the observations allows us to draw the following conclusions:

1. The spatially resolved maps do not exhibit any detectable dust polarization.
2. When we average the emission across the entire disk in a box of size  $32.7 \text{ au} \times 310 \text{ au}$ , we detect polarized dust emission at a marginally significant S/N level of 2.7, finding a polarization fraction  $P_{\text{frac}} = 0.0051 \pm 0.0019$  (i.e.,  $0.51\% \pm 0.19\%$ ). The polarization position angle  $\chi = -59.9^\circ \pm 10.6^\circ$ , i.e., it is oriented along the minor axis of the disk.
3. To improve the S/N of the observations, we transform the Stokes ( $Q$ ,  $U$ ) parameters into the ( $Q'$ ,  $U'$ ) frame such that  $\pm Q'$  correspond to polarization with an orientation along the minor axis (+) and along the major axis (−) of the disk. After doing so, we detect  $+Q'$  at a statistically significant S/N level of 3.1;  $U'$  is consistent with noise.
4. When we average the polarized emission across different regions of the disk, we find that the polarization primarily arises from the SW third of the disk; polarized emission is not detected toward the NE or central thirds.

We compare our observations with models of dust scattering and models of dust grains aligned via the radiative torque

(RAT) mechanism both with respect to the radiation flux ( $k$ -RAT) and with respect to the magnetic field ( $B$ -RAT). We find the following:

1. Polarization from scattering by dust grains can be ruled out due to the low optical depth of the  $\beta$  Pic debris disk at submillimeter wavelengths.
2. With a simple radiative transfer model we constrain the intrinsic polarization fraction of the dust grains to be  $p_0 < 1.7\%$  and  $p_0 < 1.3\%$ , assuming small grains aligned via  $k$ -RAT and  $B$ -RAT, respectively. Grains with larger  $p_0$  would produce significant polarized emission in the resolved map, which we do not detect.
3. We present synthetic observations in Figures 7 and 8, assuming  $k$ -RAT and  $B$ -RAT, respectively. Both models match our observed, full-disk-averaged polarization fraction very well. To distinguish between  $k$ -RAT and  $B$ -RAT, we average the polarized emission across the three thirds of the disk, as we do with the ALMA observations.  $B$ -RAT is excluded because it predicts too much polarization in the center third and too little polarization in the SW third (see Figure 10). We find that  $k$ -RAT is the likely mechanism producing the polarized emission in  $\beta$  Pic.
4. Given the constraint on the intrinsic polarization fraction  $p_0 < 1.7\%$ , we attempt to constrain our dust models. If the dust grains are small and perfectly aligned, they must have a very small aspect ratio of  $s < 1.025$ . For dust grains with realistic aspect ratios ( $s > 1.1$ ), the degree of alignment must be smaller than  $\sim 0.2$ , implying inefficient alignment of dust grains.
5. Based on grain-alignment timescale comparisons, the RAT alignment mechanism should be operating very well in  $\beta$  Pic, and  $k$ -RAT is favored over  $B$ -RAT. This is consistent with the conclusions we draw from the analysis of the ALMA observations and the synthetic observations.

As the first observational and theoretical analysis of deep submillimeter dust polarization observations toward a debris disk, this work paves the way for many future polarization studies of both  $\beta$  Pic and other debris disks. One path forward would be to extend our models to the regime of large ( $\sim 1$  mm) dust grains by analyzing multi-wavelength observations. Furthermore, given the fact that we were able to detect polarized dust emission when averaging across the entire disk of  $\beta$  Pic, it is likely that we would be able to make a spatially resolved polarization map if the sensitivity of the observations were improved by a factor of  $\sim 2$ . This is achievable in  $\beta$  Pic with a substantial additional investment of Band 7 observation time ( $\sim 9$  hr on-source). However, this type of deep continuum polarization observation will become more easily achievable in  $\beta$  Pic and in other (both brighter and fainter) debris disks after the ALMA 2030 wideband sensitivity upgrade is complete (Carpenter et al. 2019).





The authors thank the anonymous referee for the insightful comments. The authors acknowledge the excellent support of the EA ARC, in particular from Kazuya Saigo, Misato Fukagawa, and Álvaro González. The authors would particularly like to acknowledge the efforts of EA ARC staff member Toshinobu Takagi, who reduced the polarization data in order to confirm the results of the authors' manual reduction of the

data. The authors thank Ryo Tazaki and Alex Lazarian for fruitful discussions regarding RATs. C.L.H.H. acknowledges Patricio Sanhueza for the vibrant and helpful discussions. C.L.H.H. acknowledges the support of the NAOJ Fellowship and JSPS KAKENHI grants 18K13586 and 20K14527. A.M.H. is supported by a Cottrell Scholar Award from the Research Corporation for Science Advancement. V.J.M.L.G. acknowledges the support of the ESO Studentship Program. Z.-Y.L. is supported in part by NSF AST-1815784 and NASA 80NSSC18K1095. This paper makes use of the following ALMA data: ADS/JAO.ALMA#2019.1.00041.S. ALMA is a partnership of ESO (representing its member states), NSF (USA) and NINS (Japan), together with NRC (Canada), MOST and ASIAA (Taiwan), and KASI (Republic of Korea), in cooperation with the Republic of Chile. The Joint ALMA Observatory is operated by ESO, AUI/NRAO and NAOJ. The National Radio Astronomy Observatory is a facility of the National Science Foundation operated under cooperative agreement by Associated Universities, Inc. Some archival images of  $\beta$  Pic were retrieved from the Japanese Virtual Observatory (JVO) portal (<http://jvo.nao.ac.jp/portal>) operated by ADC/NAOJ.

*Facilities:* ALMA.

*Software:* CASA (McMullin et al. 2007). Astropy (Astropy Collaboration et al. 2018). RADMC-3D (Dullemond et al. 2012). This research made use of APLpy, an open-source plotting package for Python (Robitaille & Bressert 2012).

## ORCID iDs

Charles L. H. Hull  <https://orcid.org/0000-0002-8975-7573>  
 Haifeng Yang (杨海峰)  <https://orcid.org/0000-0002-8537-6669>  
 Paulo C. Cortés  <https://orcid.org/0000-0002-3583-780X>  
 Quentin Kral  <https://orcid.org/0000-0001-6527-4684>  
 Zhi-Yun Li  <https://orcid.org/0000-0002-7402-6487>  
 Valentin J. M. Le Gouellec  <https://orcid.org/0000-0002-5714-799X>  
 A. Meredith Hughes  <https://orcid.org/0000-0002-4803-6200>  
 Julien Milli  <https://orcid.org/0000-0001-9325-2511>  
 Richard Teague  <https://orcid.org/0000-0003-1534-5186>  
 Mark C. Wyatt  <https://orcid.org/0000-0001-9064-5598>

## References

- Ahmic, M., Croll, B., & Artymowicz, P. 2009, *ApJ*, 705, 529  
 Alves, F. O., Girart, J. M., Padovani, M., et al. 2018, *A&A*, 616, A56  
 Andersson, B. G., & Wannier, P. G. 1997, *ApJL*, 491, L103  
 Apai, D., Schneider, G., Grady, C. A., et al. 2015, *ApJ*, 800, 136  
 Arnold, J. A., Weinberger, A. J., Videen, G., & Zubko, E. S. 2019, *AJ*, 157, 157  
 Astropy Collaboration, Price-Whelan, A. M., Sipőcz, B. M., et al. 2018, *AJ*, 156, 123  
 Aumann, H. H. 1985, *PASP*, 97, 885  
 Aumann, H. H., Gillett, F. C., Beichman, C. A., et al. 1984, *ApJL*, 278, L23  
 Bacciotti, F., Girart, J. M., Padovani, M., et al. 2018, *ApJL*, 865, L12  
 Balbus, S. A., & Hawley, J. F. 1991, *ApJ*, 376, 214  
 Barnett, S. J. 1915, *PhRv*, 6, 239  
 Birstiel, T., Dullemond, C. P., Zhu, Z., et al. 2018, *ApJL*, 869, L45  
 Blandford, R. D., & Payne, D. G. 1982, *MNRAS*, 199, 883  
 Bohlin, R. C., Savage, B. D., & Drake, J. F. 1978, *ApJ*, 224, 132  
 Bohren, C. F., & Huffman, D. R. 1983, *Absorption and Scattering of Light by Small Particles* (New York: Wiley)  
 Bradley, J. P. 2003, *TrGeo*, 1, 711  
 Brandeker, A., Cataldi, G., Olofsson, G., et al. 2016, *A&A*, 591, A27

- Burlaga, L. F., Ness, N. F., McDonald, F. B., Richardson, J. D., & Wang, C. 2003, *ApJ*, **582**, 540
- Burns, J. A., Lamy, P. L., & Soter, S. 1979, *Icar*, **40**, 1
- Carpenter, J., Iono, D., Testi, L., et al. 2019, arXiv:1902.02856
- Carrasco-González, C., Henning, T., Chandler, C. J., et al. 2016, *ApJL*, **821**, L16
- Carrasco-González, C., Sierra, A., Flock, M., et al. 2019, *ApJ*, **883**, 71
- Cataldi, G., Brandeker, A., Olofsson, G., et al. 2014, *A&A*, **563**, A66
- Cataldi, G., Brandeker, A., Wu, Y., et al. 2018, *ApJ*, **861**, 72
- Cho, J., & Lazarian, A. 2007, *ApJ*, **669**, 1085
- Cortes, P. C., Le Gouellec, V. J. M., Hull, C. L. H., et al. 2021, *ApJ*, **907**, 94
- Crifo, F., Vidal-Madjar, A., Lallemand, R., Ferlet, R., & Gerbaldi, M. 1997, *A&A*, **320**, L29
- Davis, S. W., Stone, J. M., & Pessah, M. E. 2010, *ApJ*, **713**, 52
- Dent, W. R. F., Pinte, C., Cortes, P. C., et al. 2019, *MNRAS*, **482**, L29
- Dent, W. R. F., Wyatt, M. C., Roberge, A., et al. 2014, *Sci*, **343**, 1490
- Draine, B. T. 2003, *ARA&A*, **41**, 241
- Dullemond, C. P., Juhasz, A., Pohl, A., et al. 2012, RADMC-3D: A multi-purpose radiative transfer tool, Astrophysics Source Code Library, ascl:1202.015
- Fernández-López, M., Stephens, I. W., Girart, J. M., et al. 2016, *ApJ*, **832**, 200
- Gaia Collaboration, Brown, A. G. A., Vallenari, A., et al. 2018, *A&A*, **616**, A1
- Gehrels, T., Baker, L. R., Beshore, E., et al. 1980, *Sci*, **207**, 434
- Girart, J. M., Fernández-López, M., Li, Z.-Y., et al. 2018, *ApJL*, **856**, L27
- Gold, T. 1952, *MNRAS*, **112**, 215
- Goldreich, P., & Kylafis, N. D. 1981, *ApJL*, **243**, L75
- Goldreich, P., & Kylafis, N. D. 1982, *ApJ*, **253**, 606
- Gray, R. O., Corbally, C. J., Garrison, R. F., et al. 2006, *AJ*, **132**, 161
- Guillet, V., Girart, J. M., Maury, A. J., & Alves, F. O. 2020, *A&A*, **634**, L15
- Harrison, R. E., Looney, L. W., Stephens, I. W., et al. 2019, *ApJL*, **877**, L2
- Heap, S. R., Lindler, D. J., Lanz, T. M., et al. 2000, *ApJ*, **539**, 435
- Heiles, C., & Troland, T. H. 2005, *ApJ*, **624**, 773
- Henning, T., & Stognienko, R. 1996, *A&A*, **311**, 291
- Herranen, J., Lazarian, A., & Hoang, T. 2021, *ApJ*, **913**, 63
- Hoang, T., & Lazarian, A. 2009, *ApJ*, **697**, 1316
- Hughes, A. M., Duchêne, G., & Matthews, B. C. 2018, *ARA&A*, **56**, 541
- Hull, C. L. H., & Plambeck, R. L. 2015, *JAI*, **4**, 1550005
- Hull, C. L. H., Yang, H., Li, Z.-Y., et al. 2018, *ApJ*, **860**, 82
- Hull, C. L. H., Cortes, P. C., Gouellec, V. J. M. L., et al. 2020, *PASP*, **132**, 094501
- Jones, R. V., & Spitzer, L. J. 1967, *ApJ*, **147**, 943
- Kataoka, A., Muto, T., Momose, M., et al. 2015, *ApJ*, **809**, 78
- Kataoka, A., Tsukagoshi, T., Momose, M., et al. 2016, *ApJL*, **831**, L12
- Kirchschlager, F., Bertrang, G. H. M., & Flock, M. 2019, *MNRAS*, **488**, 1211
- Kral, Q., & Latter, H. 2016, *MNRAS*, **461**, 1614
- Kral, Q., Matrà, L., Wyatt, M. C., & Kennedy, G. M. 2017, *MNRAS*, **469**, 521
- Kral, Q., Wyatt, M., Carswell, R. F., et al. 2016, *MNRAS*, **461**, 845
- Lagrange, A. M., Bonnefoy, M., Chauvin, G., et al. 2010, *Sci*, **329**, 57
- Lagrange, A. M., Meunier, N., Rubini, P., et al. 2019, *NatAs*, **3**, 1135
- Lagrange, A. M., Rubini, P., Nowak, M., et al. 2020, *A&A*, **642**, A18
- Larwood, J. D., & Kalas, P. G. 2001, *MNRAS*, **323**, 402
- Lazarian, A. 2007, *J. Quant. Spec. Radiat. Transf.*, **106**, 225
- Lazarian, A., & Hoang, T. 2007a, *MNRAS*, **378**, 910
- Lazarian, A., & Hoang, T. 2007b, *ApJ*, **669**, L77
- Le Gouellec, V. J. M., Maury, A. J., Guillet, V., et al. 2020, *A&A*, **644**, A11
- Lee, C.-F., Li, Z.-Y., Ching, T.-C., Lai, S.-P., & Yang, H. 2018, *ApJ*, **854**, 56
- Lee, H. M., & Draine, B. T. 1985, *ApJ*, **290**, 211
- Li, A., & Greenberg, J. M. 1998, *A&A*, **331**, 291
- Li, D., Pantin, E., Telesco, C. M., et al. 2016, *ApJ*, **832**, 18
- Li, D., Telesco, C. M., & Wright, C. M. 2012, *ApJ*, **759**, 81
- Li, D., Telesco, C. M., Zhang, H., et al. 2018, *MNRAS*, **473**, 1427
- Liseau, R., Brandeker, A., Fridlund, M., et al. 2003, *A&A*, **402**, 183
- Mathis, J. S., Mezger, P. G., & Panagia, N. 1983, *A&A*, **500**, 259
- Matrà, L., Wyatt, M. C., Wilner, D. J., et al. 2019, *AJ*, **157**, 135
- Matrà, L., Dent, W. R. F., Wyatt, M. C., et al. 2017, *MNRAS*, **464**, 1415
- McMullin, J. P., Waters, B., Schiebel, D., Young, W., & Golap, K. 2007, in ASP Conf. Ser. 376, *Astronomical Data Analysis Software and Systems XVI*, ed. R. A. Shaw, F. Hill, & D. J. Bell (San Francisco, CA: ASP), 127
- Millar-Blanchaer, M. A., Graham, J. R., Pueyo, L., et al. 2015, *ApJ*, **811**, 18
- Miret-Roig, N., Galli, P. A. B., Brandner, W., et al. 2020, *A&A*, **642**, A179
- Mommert, M., McNeill, A., Trilling, D. E., Moskovitz, N., & Delbo', M. 2018, *AJ*, **156**, 139
- Mouillet, D., Larwood, J. D., Papaloizou, J. C. B., & Lagrange, A. M. 1997, *MNRAS*, **292**, 896
- Nagai, H., Nakanishi, K., Paladino, R., et al. 2016, *ApJ*, **824**, 132
- Naghizadeh-Khouei, J., & Clarke, D. 1993, *A&A*, **274**, 968
- Nilsson, R., Brandeker, A., Olofsson, G., et al. 2012, *A&A*, **544**, A134
- Nowak, M., Lacour, S., Lagrange, A. M., et al. 2020, *A&A*, **642**, L2
- Ohashi, S., Kataoka, A., Nagai, H., et al. 2018, *ApJ*, **864**, 81
- Ohashi, S., Kataoka, A., van der Marel, N., et al. 2020, *ApJ*, **900**, 81
- Olofsson, G., Liseau, R., & Brandeker, A. 2001, *ApJL*, **563**, L77
- Owens, M. J., & Forsyth, R. J. 2013, *LRSP*, **10**, 5
- Roberge, A., Feldman, P. D., Lagrange, A. M., et al. 2000, *ApJ*, **538**, 904
- Roberge, A., Feldman, P. D., Weinberger, A. J., Deleuil, M., & Bouret, J.-C. 2006, *Natur*, **441**, 724
- Robitaille, T., & Bressert, E. 2012, APLpy: Astronomical Plotting Library in Python, Astrophysics Source Code Library, ascl:1208.017
- Schmid, H. M., Joos, F., & Tschan, D. 2006, *A&A*, **452**, 657
- Smith, B. A., & Terrile, R. J. 1984, *Sci*, **226**, 1421
- Snellen, I. A. G., & Brown, A. G. A. 2018, *NatAs*, **2**, 883
- Stephens, I. W., Fernández-López, M., Li, Z.-Y., Looney, L. W., & Teague, R. 2020, *ApJ*, **901**, 71
- Stephens, I. W., Looney, L. W., Kwon, W., et al. 2014, *Natur*, **514**, 597
- Stephens, I. W., Yang, H., Li, Z.-Y., et al. 2017, *ApJ*, **851**, 55
- Tazaki, R., Lazarian, A., & Nomura, H. 2017, *ApJ*, **839**, 56
- Teague, R., Hull, C. L. H., Guilloteau, S., et al. 2021, *ApJ*, **922**, 139
- Telesco, C. M., Fisher, R. S., Wyatt, M. C., et al. 2005, *Natur*, **433**, 133
- van Leeuwen, F. 2007, *A&A*, **474**, 653
- Vlemmings, W. H. T., Lankhaar, B., Cazzoletti, P., et al. 2019, *A&A*, **624**, L7
- Wardle, J. F. C., & Kronberg, P. P. 1974, *ApJ*, **194**, 249
- Warren, S. G., & Brandt, R. E. 2008, *JGRD*, **113**, D14220
- Wilner, D. J., Andrews, S. M., & Hughes, A. M. 2011, *ApJL*, **727**, L42
- Yang, H. 2021, *ApJ*, **911**, 125
- Yang, H., Li, Z.-Y., Looney, L., & Stephens, I. 2016a, *MNRAS*, **456**, 2794
- Yang, H., Li, Z.-Y., Looney, L. W., et al. 2016b, *MNRAS*, **460**, 4109
- Yang, H., Li, Z.-Y., Stephens, I. W., Kataoka, A., & Looney, L. 2019, *MNRAS*, **483**, 2371
- Zagorovsky, K., Brandeker, A., & Wu, Y. 2010, *ApJ*, **720**, 923
- Zhu, Z., Zhang, S., Jiang, Y.-F., et al. 2019, *ApJL*, **877**, L18
- Zwintz, K., Reese, D. R., Neiner, C., et al. 2019, *A&A*, **627**, A28